

# Structural and mechanistic insights into the interaction of the circadian transcription factor BMAL1 with the KIX domain of the CREB-binding protein

Received for publication, June 18, 2019, and in revised form, August 30, 2019 Published, Papers in Press, September 12, 2019, DOI 10.1074/jbc.RA119.009845

Archit Garg<sup>‡§1</sup>, Roberto Orru<sup>§</sup>, Weixiang Ye<sup>¶</sup>, Ute Distler<sup>||</sup>, Jeremy E. Chojnacki<sup>\*\*</sup>, Maja Köhn<sup>\*\*2</sup>, Stefan Tenzer<sup>||</sup>, Carsten Sönnichsen<sup>¶</sup>, and Eva Wolf<sup>‡§3</sup>

From the <sup>‡</sup>Institute of Molecular Biology (IMB), Ackermannweg 4, 55128 Mainz, Germany, the <sup>§</sup>Institute of Molecular Physiology, Johannes Gutenberg-University of Mainz, 55128 Mainz, Germany, the <sup>¶</sup>Institute of Physical Chemistry, Johannes Gutenberg-University of Mainz, Duesbergweg 10–14, 55128 Mainz, Germany, the <sup>||</sup>Institute of Immunology, University Medical Center of the Johannes-Gutenberg University Mainz, 55131 Mainz, Germany, and the <sup>\*\*</sup>European Molecular Biology Laboratory, 69117 Heidelberg, Germany

Edited by Joel M. Gottesfeld

The mammalian CLOCK:BMAL1 transcription factor complex and its coactivators CREB-binding protein (CBP)/p300 and mixed-lineage leukemia 1 (MLL1) critically regulate circadian transcription and chromatin modification. Circadian oscillations are regulated by interactions of BMAL1's C-terminal transactivation domain (TAD) with the KIX domain of CBP/p300 (activating) and with the clock protein CRY1 (repressing) as well as by the BMAL1 G-region preceding the TAD. Circadian acetylation of Lys<sup>537</sup> within the G-region enhances repressive BMAL1-TAD-CRY1 interactions. Here, we characterized the interaction of the CBP-KIX domain with BMAL1 proteins, including the BMAL1-TAD, parts of the G-region, and Lys<sup>537</sup>. Tethering the small compound 1–10 in the MLL-binding pocket of the CBP-KIX domain weakened BMAL1 binding, and MLL1-bound KIX did not form a ternary complex with BMAL1, indicating that the MLL-binding pocket is important for KIX-BMAL1 interactions. Small-angle X-ray scattering (SAXS) models of BMAL1 and BMAL1:KIX complexes revealed that the N-terminal BMAL1 G-region including Lys<sup>537</sup> forms elongated extensions emerging from the bulkier BMAL1-TAD:KIX core complex. Fitting high-resolution KIX domain structures into the SAXS-derived envelopes suggested that the G-region emerges near the MLL-binding pocket, further supporting a role of this pocket in BMAL1 binding. Additionally, mutations in the second CREB-pKID/c-Myb-binding pocket of the KIX domain moderately impacted BMAL1 binding. The BMAL1(K537Q) mutation mimicking Lys<sup>537</sup> acetylation, however, did not affect the KIX-binding affinity, in contrast to its enhancing

effect on CRY1 binding. Our results significantly advance the mechanistic understanding of the protein interaction networks controlling CLOCK:BMAL1- and CBP-dependent gene regulation in the mammalian circadian clock.

Most organisms possess circadian rhythms coordinated by circadian clocks that synchronize them to the 24-h light-dark cycle. In mammals, circadian rhythmicity is controlled by transcriptional/translational feedback loops. The core transcriptional/translational feedback loop consists of the heterodimeric basic helix-loop-helix (bHLH)<sup>4</sup>-PER-ARNT-SIM (PAS) domain-containing transcriptional activators CLOCK (circadian locomotor output cycle kaput) and BMAL1 (brain and muscle ARNT-like protein-1), which circadianly regulate genes encoding Period (PER1, PER2, and PER3) and Cryptochrome (CRY1 and CRY2) clock proteins as well as many clock-controlled genes (1, 2). Analyses in mouse liver led to a model of three temporally separated states of CLOCK:BMAL1-dependent circadian transcription: an early repressive state, a late repressive state, and an active state (3). Large multisubunit PER- and CRY-containing complexes interact with CLOCK:BMAL1 in the early phase of repression (4), whereas CRY1 alone maintains the late repressive state (5, 6). In the active state, CLOCK:BMAL1 associates with co-activators such as the histone acetyl transferase CREB-binding protein (CBP) and its paralog p300, which acetylate histone H3 Lys<sup>9</sup>/Lys<sup>14</sup> (7).

BMAL1 is a key regulator of the circadian clock as documented by the loss of molecular and behavioral circadian rhythmicity in BMAL1<sup>−/−</sup> knockout mice (8). The C-terminal transactivation domain (TAD) of BMAL1 (Fig. 1A) is required for circadian cycling, and mutations in the TAD affect the circadian period (9). Additionally, the BMAL1 region preceding the TAD (termed G-region, Glu<sup>429</sup>–Ile<sup>578</sup>) critically affects circa-

The authors declare that they have no conflicts of interest with the contents of this article.

This article contains Table S1 and Figs. S1–S7.

The SAXS scattering data collected at the P12 beamline has been deposited in the Small Angle Scattering Biological Data Bank (SASBDB) with the accession codes SASDF27, SASDF37, SASDF47, SASDF57, SASDF67, and SASDF77.

<sup>1</sup> Affiliated with and financially supported by the International Ph.D. Programme on Gene Regulation, Epigenetics, and Genome Stability, Mainz, Germany.

<sup>2</sup> Present address: Faculty of Biology and Signalling Research Centers BIOS and CIBSS, Albert-Ludwigs-University of Freiburg, Schänzlestr. 18, D-79104 Freiburg, Germany.

<sup>3</sup> To whom correspondence should be addressed: Institute of Molecular Biology and Institute of Molecular Physiology, Johannes Gutenberg-University of Mainz, Ackermannweg 4, 55128 Mainz, Germany. Tel.: 49-6131-39-21701; E-mail: ewawolf1@uni-mainz.de.

<sup>4</sup> The abbreviations used are: bHLH, basic helix-loop-helix; PAS, PER-ARNT-SIM; CBP, CREB-binding protein; CREB, cAMP-response element-binding protein; FWHM, full width at half-maximum; TAD, transactivation domain; MLL, mixed lineage leukemia; pKID, phosphorylated kinase-inducible domain; SAXS, small-angle X-ray scattering; NanoSPR, nano-surface plasmon resonance; MST, microscale thermophoresis; FP, fluorescence polarization; PDB, Protein Data Bank; NTA, nitrilotriacetic acid.

dian luminescence rhythms of a  $\text{Per2}^{\text{Luc}}$  reporter in rescued  $\text{BMAL1}^{-/-}$   $\text{Per2}^{\text{Luc}}$  fibroblasts (9). Furthermore, homozygous mutant mice with a C-terminally truncated  $\text{BMAL1}(1-537)$  variant lacking the TAD and part of the G-region lose circadian rhythmicity (10). The  $\text{BMAL1}$ -TAD region is suggested to act as a regulatory switch between a transcriptionally repressing “off” mode and an activating “on” mode, bound to  $\text{CRY1}$  or to co-activators, respectively (11, 12). Furthermore,  $\text{BMAL1}$  is specifically acetylated at  $\text{Lys}^{537}$  within the  $\text{BMAL1}$  G-region in a daily rhythmic manner *in vivo*, which enhances the  $\text{BMAL1}$ - $\text{CRY}$  interaction and subsequent transcriptional repression of  $\text{CLOCK}:\text{BMAL1}$  (13). Consistently, the acetyl-lysine mimetic  $\text{BMAL1 K537Q}$  mutation increases the binding affinity of purified  $\text{BMAL1}$  to  $\text{CRY1}$  *in vitro* by unmasking negative charges in the  $\text{BMAL1}$ -TAD (14, 15). Interestingly,  $\text{CRY1}$  and  $\text{CBP}$  compete for binding to the  $\text{BMAL1}$ -TAD (9). An IXXLL motif in a predicted  $\alpha$ -helix located within the  $\text{BMAL1}$ -TAD (residues 602–606, numbering according to  $\text{BMAL1b}(1-625)$  isoform used herein) (Fig. 1, A and B), and the seven most C-terminal  $\text{BMAL1}$  residues participate in binding of the KIX (kinase-inducible domain-interacting) domain of  $\text{CBP}$  (9) and of the cryptochromes ( $\text{CRY1}/2$ ) (14). Deletion of the last seven residues decreases the  $\text{BMAL1}$ -TAD affinity for the KIX domain and for  $\text{CRY1}$  by 2–3-fold and shortens the circadian period by  $\sim 3$  h, whereas the double mutation  $\text{L605A}/\text{L606A}$  within the IXXLL motif abolishes circadian cycling and disrupts the interaction of  $\text{BMAL1}$  with KIX and with  $\text{CRY1}$  (9). Furthermore, there is a conformational switch in the distal C terminus of the  $\text{BMAL1}$ -TAD in the form of a  $\text{Trp}^{623}$ – $\text{Pro}^{624}$  imide bond that undergoes *cis-trans* isomerization accelerated by peptidyl prolyl isomerases (16). Locking the switch to either a *cis*- or *trans*-conformation affects the circadian period but does not alter the  $\text{BMAL1}$  affinity for the KIX domain or  $\text{CRY1}$  (16).

$\text{CBP}$  and  $\text{p300}$  are paralog transcriptional regulators possessing similar multidomain architectures and histone acetyltransferase activities (17, 18). Their highly conserved KIX domain (Fig. 1C and Fig. S1, A and B) interacts with a number of transcription factors, such as breast cancer 1 ( $\text{BRCA1}$ ),  $\text{c-Jun}$ ,  $\text{FOXO3a}$ ,  $\text{p53}$ , mixed lineage leukemia (MLL) protein 1,  $\text{c-Myb}$ ,  $\text{CREB}$ , and  $\text{BMAL1}$  (19). Two distinct KIX-binding sites referred to as MLL- and  $\text{c-Myb}/\text{CREB}$ - $\text{pKID}$ -binding sites are typically targeted by intrinsically disordered regions within TADs of the binding partners, which frequently include a  $\Phi\text{XX}\Phi\Phi$  motif (where  $\Phi$  represents a hydrophobic residue) and attain folding upon complexation (19–24). Notably, KIX can bind different transcription factors to its two binding pockets allosterically (25, 26). For example, MLL1 binding to the MLL pocket enhances the affinity of the  $\text{Ser}^{133}$ -phosphorylated kinase-inducible domain ( $\text{pKID}$ ) of  $\text{CREB}$  and of  $\text{c-Myb}$  to the second KIX-binding pocket (26). Furthermore, covalent tethering of the small molecule 1–10 (Fig. 1C) to  $\text{Leu}^{664}$  or  $\text{Asn}^{627}$  within the MLL-binding pocket of KIX significantly reduces the MLL1-binding affinity by a factor of about 100 (27) but also imparts positive (1–10-KIX(N627C)) or negative (1–10-KIX(L664C)) cooperativity for  $\text{pKID}$  binding to the second KIX-binding pocket (28). The transcription factors  $\text{FOXO3a}$  (29) and  $\text{p53}$  (30), on the other hand, possess two KIX-binding regions with  $\Phi\text{XX}\Phi\Phi$  motifs

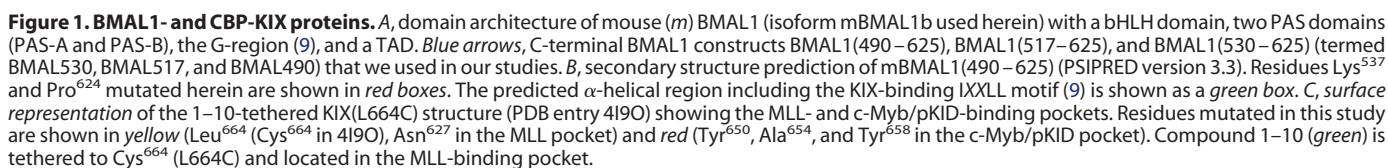
to target both the MLL and the  $\text{pKID}/\text{c-Myb}$  pockets in a cooperative manner.

The amount of  $\text{CBP}$  protein present *in vivo* is limiting. Therefore, binding competition of different transcriptional regulators is crucial to define and regulate the diverse biological functions of  $\text{CBP}$  (17). Interestingly, the KIX ligands MLL1 and  $\text{CREB}$  also play important roles in the regulation of circadian transcription (31–33). MLL1 co-activates circadian genes by daily rhythmic recruitment to  $\text{CLOCK}:\text{BMAL1}$  and cyclic H3  $\text{Lys}^4$  trimethylation, and this MLL1 activity is further enhanced by  $\text{p300}/\text{CBP}$ -dependent MLL1 acetylation (32, 33).  $\text{CREB}$ - $\text{CBP}$  interactions, on the other hand, are essential for light entrainment of the circadian master clock in the suprachiasmatic nucleus via up-regulation of the *per1* clock gene, which contains  $\text{CLOCK}:\text{BMAL1}$ - and  $\text{CREB}$ -binding sites in its promoter (34, 35). These observations suggest a functional interplay of  $\text{CBP}$ ,  $\text{BMAL1}$ , MLL1, and  $\text{CREB}$  within circadian gene regulation, chromatin modification, and light entrainment, which, at a mechanistic level, is far from understood. Whereas the KIX- and  $\text{CRY}$ -binding  $\text{BMAL1}$ -TAD regions have been described (9, 14), the binding sites of the  $\text{BMAL1}$ -TAD within the KIX domain and the interplay of  $\text{BMAL1}$  with other KIX ligands are largely undefined. Here, we purified three C-terminal  $\text{BMAL1}$  constructs including the  $\text{BMAL1}$ -TAD and parts of the G-region to unravel the mechanisms underlying their interaction with the  $\text{CBP}$ -KIX domain. We show that tethering the KIX domain with the small molecule 1–10 in the MLL-binding pocket lowers its affinity for  $\text{BMAL1}$ , suggesting a role of this pocket in  $\text{BMAL1}$  binding. In a pulldown experiment, MLL1 sequestered KIX from a preformed KIX: $\text{BMAL1}$  complex, and therefore a ternary MLL1-TAD: $\text{BMAL1}$ -TAD: $\text{CBP}$ -KIX complex could not be formed. Moreover, mutations within the  $\text{c-Myb}/\text{pKID}$ -binding pocket of KIX decreased the affinity for  $\text{BMAL1}$ , suggesting that both KIX-binding pockets are involved in  $\text{BMAL1}$  interactions. Furthermore, we showed that the  $\text{BMAL1}(\text{K537Q})$  mutant mimicking lysine acetylation does not alter the  $\text{BMAL1}$  affinity for KIX, contrary to its enhancing effect on the repressive  $\text{CRY1}$ - $\text{BMAL1}$  interaction (13, 14). Our CD spectra suggest that  $\text{BMAL1}$  does not become structured upon complexation with KIX, which contrasts with the binding-induced folding reported for other KIX ligands (19, 20, 23). Finally, we present small-angle X-ray scattering (SAXS) models of  $\text{BMAL1}$  and three  $\text{BMAL1}:\text{KIX}$  complexes, which depict the  $\text{BMAL1}$  regions N-terminal to the TAD including  $\text{Lys}^{537}$  and parts of the G-region emerging from one side of the  $\text{BMAL1}$ -TAD: $\text{KIX}$  core complex, thereby suggesting a directionality for the  $\text{BMAL1}$ -TAD- $\text{CBP}$ -KIX interactions.

## Results

### Defining $\text{BMAL1}:\text{CBP}$ -KIX complexes for SAXS analyses and interaction studies

We initially purified the complex of the mouse  $\text{CBP}$ -KIX domain (residues 586–672) with the previously described  $\sim 14$ -kDa C-terminal mouse  $\text{BMAL1}(490-625)$  fragment (termed  $\text{BMAL490}$ ) that includes the  $\text{BMAL1}$ -TAD,  $\text{Lys}^{537}$ , and parts of the  $\text{BMAL1}$  G-region (14) (Fig. 1). Limited proteolysis of the purified  $\text{BMAL1}(490-625):\text{KIX}$  complex revealed



### *Tethering compound 1–10 in the MLL-binding pocket of KIX reduces the BMAL1-TAD affinity*

To analyze the role of the MLL-binding pocket of KIX in BMAL1 interactions, we introduced the mutations L664C and N627C on opposite sides of the MLL-binding pocket and tethered compound 1–10 to Cys<sup>664</sup> or Cys<sup>627</sup> (Fig. 1C). Using MS, we showed that tethering was >97% and >99% complete for KIX(L664C) and KIX(N627C), respectively (Figs. S2 and S3). We then performed MST and fluorescence polarization (FP) experiments to determine the effect of mutations L664C and N627C and of compound 1–10 on the binding affinities of BMAL530(P624A) (Fig. 2). For MST and FP analyses, purified BMAL1 was fluorescently labeled on its N-terminal His<sub>6</sub> tag, and increasing concentrations of KIX proteins (WT KIX, KIX(L664C), 1–10-KIX(L664C), KIX(N627C), or 1–10-KIX(N627C)) were titrated to labeled BMAL1. In both our MST and FP experiments, the WT KIX domain bound to BMAL1 with



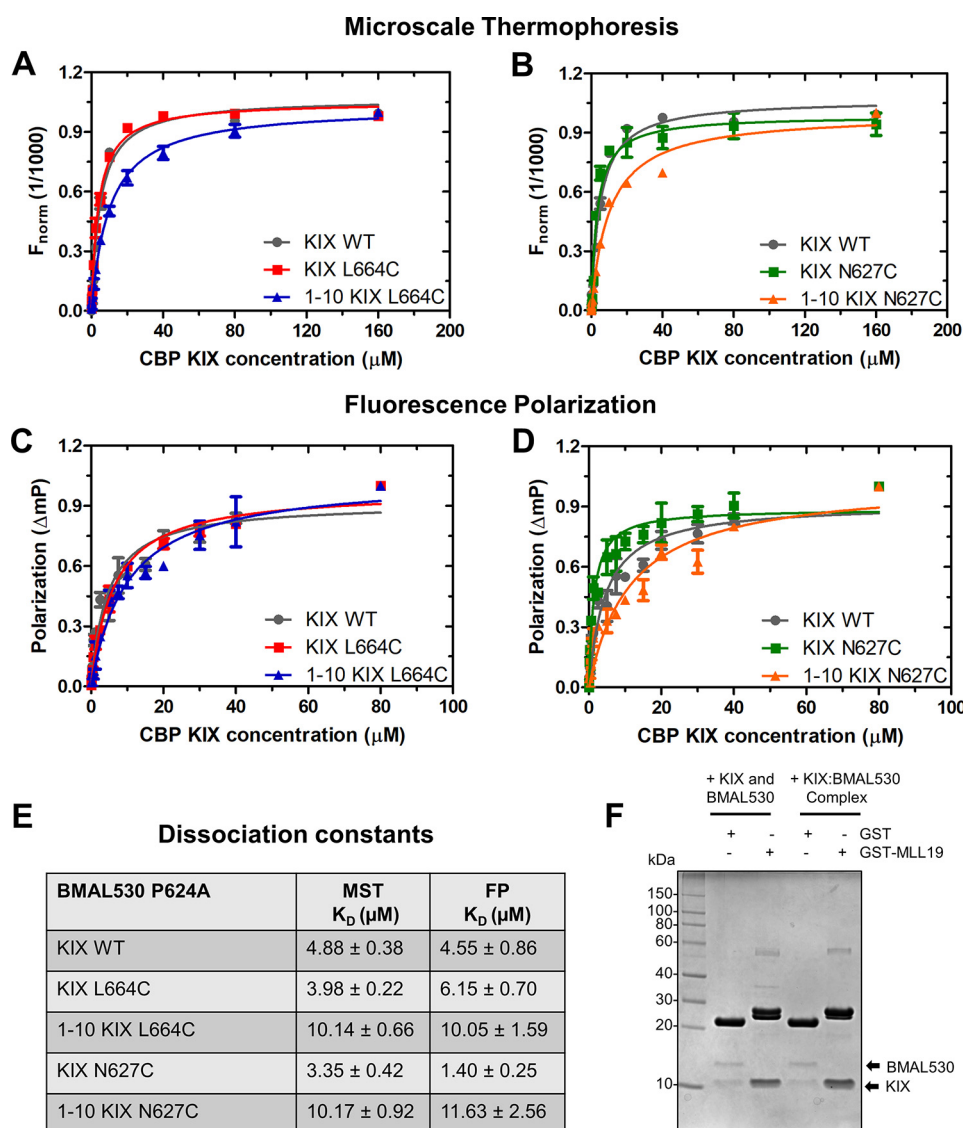


**Figure 2. Analysis of BMAL1-KIX domain interactions by MST, FP, and GST pulldown.** A and B, MST analyses of the interaction of His<sub>6</sub>-BMAL530(P624A) (concentration: 0.05  $\mu$ M, His tag fluorescently labeled with RED-tris-NTA NT-647 dye) with increasing concentrations (0.005–160  $\mu$ M) of WT KIX and KIX mutant L664C (A) or N627C (B) untethered and tethered with compound 1–10. C and D, FP affinity measurements of KIX WT and untethered/1–10-tethered KIX(L664C) (C) or KIX(N627C) (D) (concentration range 0.04–80  $\mu$ M) with 0.05  $\mu$ M RED-tris-NTA-labeled His<sub>6</sub>-BMAL530(P624A). The normalized fluorescence (MST) or polarization (FP) values were plotted against the ligand concentration, and best fits were obtained using a one-site binding model. A  $\sim$ 2-fold lower BMAL1 affinity of 1–10-tethered KIX is observed with both methods, suggesting a role of the MLL-binding pocket in BMAL1 interactions. E, dissociation constants ( $K_D$ ) for BMAL1-KIX interactions obtained from MST and FP. The values are the mean of two or three independent measurements. F, GST pulldown assay of KIX and BMAL530 (prey) with the MLL1-TAD peptide (GST-MLL19, bait). The inability of MLL1-bound KIX to retain BMAL1 in a ternary MLL1:KIX:BMAL1 complex confirms the importance of the MLL-binding pocket in BMAL1:KIX complex formation. Error bars, S.E.

about 5  $\mu$ M affinity. Notably, this affinity is somewhat lower than reported previously (16), possibly due to interference of the N-terminal BMAL1-His<sub>6</sub> tag or the RED-tris-NTA NT-647 fluorescent dye. Compared with WT KIX, the affinity of the untethered KIX(N627C) mutant protein to BMAL1 was 1.5-fold higher in MST and 3-fold higher in FP, whereas the L664C mutation showed a 1.5-fold reduced affinity in FP (Fig. 2). Tethering compound 1–10 to Cys<sup>664</sup> or Cys<sup>627</sup> reduced the BMAL1-binding affinity by about 2–2.5-fold compared with WT KIX in both our MST (Fig. 2, A, B, and E) and FP (Fig. 2, C–E) measurements, resulting in a BMAL1 affinity of about 10  $\mu$ M to both 1–10-KIX(L664C) and 1–10-KIX(N627C). These results suggest that the MLL-binding pocket plays a role in the interaction of KIX with BMAL1.

### MLL1 displaces BMAL1 from a BMAL1:KIX complex

We purified a GST-tagged MLL1-TAD peptide (denoted as MLL19) of the MLL1 transactivation domain (TAD) that was used previously for quantitative biophysical and structural analyses of KIX-MLL1-TAD interactions (25, 26). We performed a GST pulldown assay with GST-MLL19 as bait using either the purified preformed BMAL530:KIX complex as prey or simultaneously adding the two individually purified BMAL530 and KIX proteins as prey (Fig. 2F). Interestingly, MLL19 only pulled down KIX, but not BMAL1, when incubated with both KIX and BMAL1 proteins (Fig. 2F, lane 3), and MLL19 even sequestered KIX when incubated with the preformed BMAL1:KIX complex (Fig. 2F, lane 5). Notably, this

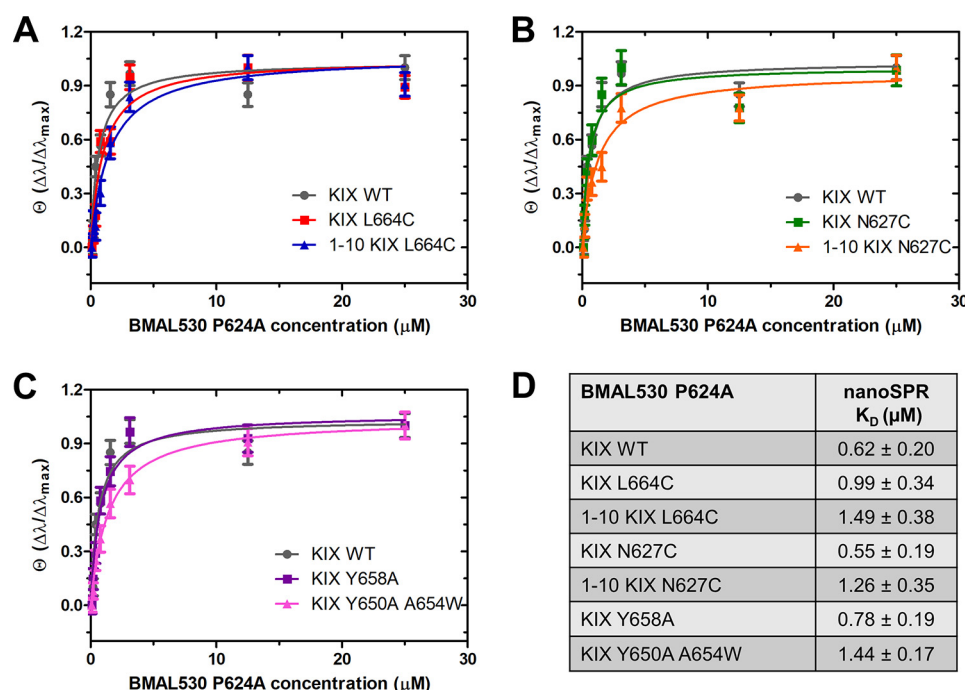


**Figure 3. Analyses of BMAL1-KIX interactions by NanoSPR.** A–C, Ni-NTA functionalized gold nanorods were covered with the following His<sub>6</sub>-tagged KIX receptor proteins: WT KIX (A–C), compound 1–10-tethered/untethered KIX(L664C) (A), 1–10-tethered/untethered KIX(N627C) (B), and KIX(Y658A) and KIX(Y650A/A654W) mutated in the c-Myb/pKID-binding pocket (C). Increasing concentrations of untagged BMAL530(P624A) (0.01–25  $\mu\text{M}$ ) were flushed into the flow cell, and plasmon resonance wavelength shifts ( $\Delta\lambda_{\text{res}}$ ) were recorded. The data points correspond to the normalized mean plasmon shift  $\Delta\lambda_{\text{res}}$  measured on 80–200 nanoparticles for each receptor. Error bars, S.E. The best fits were obtained using a one-site binding model. D, dissociation constants ( $K_D$ ) obtained from NanoSPR measurements. Compound 1–10 lowers the affinity of KIX for BMAL1 about 2-fold, consistent with our MST and FP measurements (Fig. 2). Mutations in the c-Myb/pKID-binding pocket also destabilize the KIX-BMAL1 interaction, suggesting that both KIX-binding pockets play a role in BMAL1 interactions.

effect was not observed in control pulldowns using GST only (Fig. 2F, lanes 2 and 4). Hence, a ternary complex between the BMAL1-TAD, the MLL1-TAD, and the CBP-KIX domain could not be formed under our pulldown conditions, which further supports the importance of the MLL-binding pocket for BMAL1 interactions.

#### Mutations in the MLL- and c-Myb/CREB-pKID-binding pocket of KIX affect BMAL1 binding

To further confirm the role of the MLL-binding pocket and to characterize the impact of the second c-Myb/CREB-pKID-binding pocket on KIX-BMAL1 interactions, we also determined the effect of compound 1–10 and of mutations in both KIX domain pockets on BMAL1-binding affinities using single plasmonic nanoparticles as nanosensors, a technique termed NanoSPR, in analogy to the established and related surface plasmon resonance (SPR) method (36–38). The NanoSPR technique was used for the comparative analysis of both KIX binding pockets, as it allowed us to measure the effects of 1–10 tethering and of all of our mutations in the MLL- and c-Myb/pKID-binding pockets simultaneously within one titration experiment to make them internally comparable. In this NanoSPR experiment, nanoparticles functionalized with N-terminally His-tagged WT or mutant KIX proteins were utilized as sensors. Increasing concentrations of the untagged BMAL530(P624A) protein were passed through the flow cell until the interaction reached equilibrium. Thereby wavelength shifts of about 1400 nanoparticles were measured to obtain 80–200 data points (particles) (*i.e.* high statistics) for each WT

or mutant KIX protein. Collectively, NanoSPR enabled us to also measure moderate (*e.g.* 2-fold) BMAL1 affinity changes caused by alterations in the two KIX-binding pockets within the same experiment with high statistics and using relatively low amounts of unlabeled proteins. In our NanoSPR experiment, the WT KIX domain was found to bind BMAL1 with an affinity of  $\sim 0.6 \mu\text{M}$ , which is in the range determined in a previous study (16), likely because BMAL1 was not N-terminally His-tagged or labeled. The L664C mutation in the MLL-binding pocket weakened the BMAL1 affinity by about 1.5-fold, whereas the N627C mutation showed nearly WT behavior (Fig. 3, A, B, and D). Tethering compound 1–10 to either Cys<sup>664</sup> or Cys<sup>627</sup> reduced the BMAL1 affinity by about 2-fold compared with WT KIX, resulting in affinities of  $\sim 1.5$  and  $\sim 1.3 \mu\text{M}$  for 1–10-KIX(L664C) and 1–10-KIX(N627C), respectively. These results are in qualitative agreement with our MST and FP measurements and provide further evidence that the MLL-binding pocket plays a role in the KIX-BMAL1 interaction. Notably, compound 1–10 weakens the binding of MLL1 to the KIX domain much more significantly, reducing MLL1-TAD affinity by about 100-fold (27), suggesting that BMAL1 uses a binding mode different from that used by MLL1. Furthermore, BMAL1 binding may be stabilized by additional binding interfaces (*e.g.* in the second KIX-binding pocket).

To analyze the role of the second c-Myb/pKID-binding pocket in BMAL1 interactions, we used NanoSPR to determine BMAL1-binding affinities to KIX proteins with a single Y658A and a double Y650A/A654W mutation in the shallow groove of this pocket (Figs. 1C and 3C). The mutations were chosen based

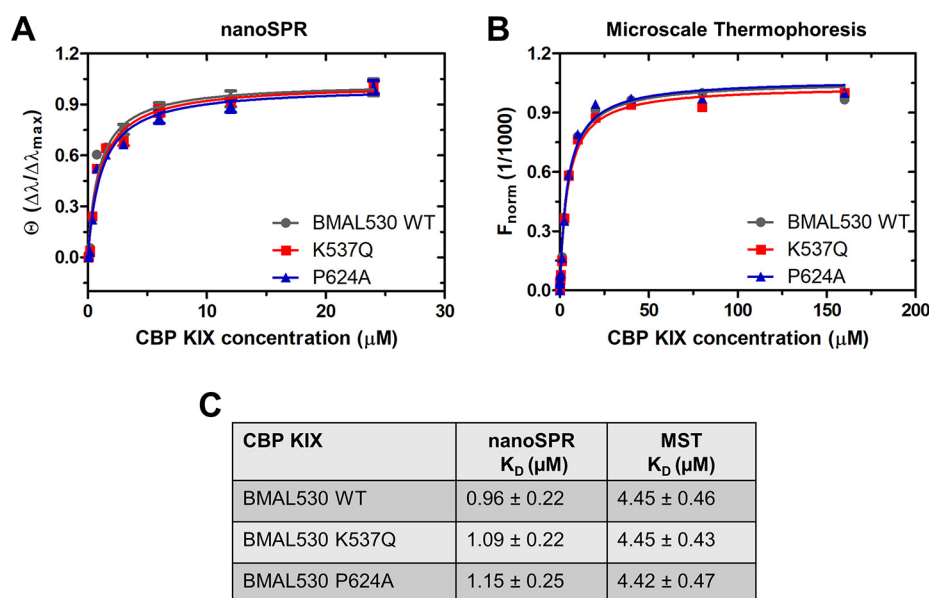


**Figure 4. The K537Q mutation mimicking Lys<sup>537</sup> acetylation of BMAL1 does not affect KIX-binding affinity.** A, affinity analysis using NanoSPR. Data points correspond to the normalized mean plasmon shift  $\Delta\lambda_{res}$  measured on 30–50 nanoparticles covered by His<sub>6</sub>-BMAL530 WT or P624A and K537Q mutants titrated with increasing concentrations of WT KIX (0.04–25 μM). Error bars, S.E. B, affinity analysis by MST. Increasing KIX concentrations (0.005–160 μM) were titrated against 50 nM fluorescently labeled His<sub>6</sub>-BMAL530 WT or P624A and K537Q mutants. The normalized fluorescence was plotted against the ligand concentration, and best fits were obtained using a one-site binding model. C, dissociation constants obtained from NanoSPR and MST measurements. The P624A mutation locking the Trp<sup>623</sup>–Pro<sup>624</sup> imide bond in its *trans*-conformation does not affect the KIX-binding affinity of BMAL1 as described previously (13). The identical affinities of KIX for BMAL530 WT and BMAL1(K537Q) indicated no effect of BMAL1 acetylation on its interaction with the KIX domain.

on their ability to significantly reduce the binding affinity of the KIX domain for c-Myb and pKID (21). Both mutant KIX proteins retained their secondary structure, as shown by CD spectra (Fig. S4). Different from the strong impact of Tyr<sup>650</sup>, Ala<sup>654</sup>, and Tyr<sup>658</sup> mutations on c-Myb and pKID binding (21), the Y650A/A654W double mutation lowered the affinity of KIX for BMAL1 by 2–2.5-fold, whereas even less pronounced effects were observed for the Y658A mutant (Fig. 3, C and D). However, comparably moderate effects were reported for mutations in the MLL pocket (I660A/L664A double mutant) or the c-Myb/pKID pocket (Y650A/A654Q/Y658A triple mutant) on the affinity of FOXO3a, which was shown by NMR solution structures to bind to both KIX pockets in two different orientations (29). Based on our interaction studies and reminiscent of FOXO3a, we therefore propose that both KIX-binding pockets play a role in KIX-BMAL1 interactions, and BMAL1 may exploit the KIX pockets in a different manner than MLL1, pKID, and c-Myb.

#### The acetyl-lysine mimetic BMAL1 K537Q mutation does not affect the BMAL1-KIX binding affinity

BMAL1 acetylation at Lys<sup>537</sup> enhances CRY1 binding to BMAL1 and transcriptional repression of CLOCK:BMAL1 *in vivo* (13). The acetyl-lysine mimetic K537Q mutation in the purified BMAL1 protein mirrors the *in vivo* effect of Lys<sup>537</sup> acetylation by increasing the CRY1-binding affinity to the BMAL1-TAD (14, 15). As Lys<sup>537</sup> acetylation is daily rhythmic in mouse liver, peaking in the repressive phase (13), we hypothesized that CBP-KIX may preferentially bind to nonacetylated BMAL1 during the transcriptionally active phase. This prompted us to analyze the effect of the acetyl-lysine mimetic BMAL1 K537Q mutation on the binding affinity of KIX to test whether this

mutation weakens KIX binding *in vitro*. However, using NanoSPR and MST, we found that WT BMAL530 and the BMAL530(K537Q) mutant bound to the KIX domain with similar affinities (Fig. 4, A–C). Hence, the K537Q mutation does not affect binding of BMAL1 to the KIX domain, in contrast to the enhanced BMAL1(K537Q)-CRY1 interaction. Likewise, the P624A mutation locking the Trp<sup>623</sup>–Pro<sup>624</sup> imide bond at the BMAL1 C terminus in the *trans* conformation does not affect BMAL1 affinity for KIX (Fig. 4), as reported previously (16). We propose that the somewhat lower ~1 μM binding affinity of BMAL530 (WT, P624A, K537Q) to WT KIX determined in this NanoSPR experiment (Fig. 4) compared with the experiment shown in Fig. 3 is correlated with the fact that now N-terminally His<sub>6</sub>-tagged BMAL1 is used as surface-bound receptor, consistent with the overall lower KIX-binding affinities of N-terminally labeled and His<sub>6</sub>-tagged BMAL1 observed in MST and FP (Fig. 2). Hence, manipulation of the N-terminal end of BMAL530 appears to affect KIX interactions, but this is unrelated to the modification of Lys<sup>537</sup>.

#### KIX binding does not induce the formation of extended regular secondary structures in BMAL1

The secondary structure of the purified BMAL530 and KIX proteins and their folding behavior upon complex formation were analyzed using CD spectroscopy. The KIX domain was determined to be mostly helical (~58%), consistent with known NMR and crystal structures (20, 27, 39), whereas BMAL1 was mostly unstructured and intrinsically disordered (~70%) with a local tendency toward α-helix (Fig. 5A and Table 1), which agrees with previous reports (9, 14). Interestingly, we did not observe pronounced changes in the secondary structure content of the BMAL530:KIX complex over a course of time rang-



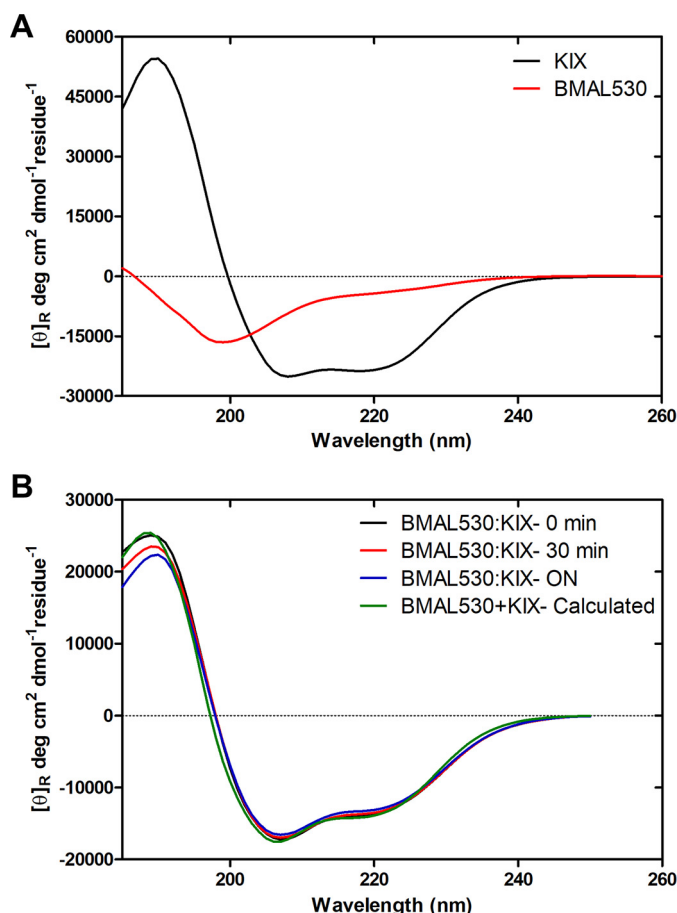


**Figure 5. BMAL1 does not fold upon binding to KIX.** A, individual CD spectra of the KIX domain and BMAL530 show well-folded secondary structure for KIX and a mostly disordered conformation for BMAL1 consistent with previous reports (14, 20, 27, 39). B, incubation of BMAL530 with KIX for a period of 30 min to overnight (ON; ~17 h) after mixing at time point 0 min does not suggest major folding of BMAL1 upon complexation, as indicated by almost identical spectra in the 208- and 222-nm region and high similarity of experimental and calculated complex spectra. The molar ellipticity per residue ( $MRE, [\theta]_R$ ) is plotted against the wavelength. The calculated (BMAL530 + KIX) CD spectrum is the result of the averaged CD spectra of individual BMAL530 and KIX proteins.

ing from 30 min to overnight (~17 h) after mixing the individually purified KIX and BMAL1 proteins (Fig. 5B and Table 1). Moreover, the experimental CD spectra of the BMAL530:KIX complex are close to the calculated average of the secondary structure contents of the individual BMAL1 and KIX proteins. Hence, our CD spectra do not suggest the formation of extended regular secondary structures in BMAL1 upon KIX binding, unlike the structuring of pKID and c-Myb induced by KIX binding (20, 23). However, based on our CD spectra, we cannot exclude conformational rearrangements associated with minor secondary structure changes (e.g. locally enhanced helix formation). We note that our MST and FP interaction measurements (Figs. 2 and 4B) were performed after a 30-min co-incubation of BMAL1 and KIX at each titrant concentration, and comparable results were obtained after 2-h and overnight co-incubation. Therefore, BMAL1-KIX binding occurs within 30 min, and the lack of pronounced secondary structure changes suggested by our CD spectra is not due to a lack of BMAL1-KIX interactions.

### Analyses of the BMAL1:KIX complex architecture by SAXS

To analyze the shapes, dimensions, folding, and conformational flexibility of the individual BMAL1 and KIX proteins and their complexes, we performed in-solution SAXS measurements of our purified BMAL530(P624A) protein, of the KIX domain (KIX(L664C) untethered and 1–10-tethered), and of three BMAL1:KIX complexes including the BMAL1 constructs BMAL1(530–625)P624A (BMAL530:KIX), BMAL1(517–625) (BMAL517:KIX), or BMAL1(490–625) (BMAL490:KIX) (Table S1). The Guinier analysis of our SAXS data indicated that all of our samples were free of aggregates (Figs. S5B, S6C, and S7B). Furthermore, the estimated molecular weights that were calculated using a Bayesian approach (40) are consistent with a 1:1 stoichiometry of the BMAL1:KIX complexes (Table 2). The Kratky plot suggests that BMAL530 is mostly unfolded and elongated in shape (Fig. S6B), whereas the BMAL1:KIX complexes are partially unfolded and elongated in shape (Figs. S6B and S7A). Consistent with our CD spectra (Fig. 5 and Table 1), we attribute the partial folding of the BMAL1:KIX complexes to contributions of both the helically folded KIX domain and the mostly unstructured BMAL1 fragments. From the distance distribution curves, the maximum particle dimension ( $D_{max}$ ) was calculated to be 110 Å for BMAL530 and 64 Å for the tethered and 81 Å for the untethered KIX domain (Fig. 6A, Fig. S5C, and Table 2). These dimensions are consistent with a more elongated shape of BMAL530 compared with the more compact KIX domain and also with the enhanced conformational stability of the 1–10-tethered KIX domain compared with untethered KIX (28). The maximum particle dimensions ( $D_{max}$ ) for the BMAL530:KIX, BMAL517:KIX, and BMAL490:KIX complexes were calculated to be 115, 137, and 175 Å, respectively (Figs. 6A and 7A). We attribute the elongated shapes and maximum dimensions ( $D_{max}$ ) of the complexes to the BMAL1 proteins, which, as our CD and SAXS data suggest, remain largely unstructured in the complexes and extend beyond the more compact KIX domain.

Based on our SAXS data, we calculated low-resolution models for KIX, BMAL530, and the BMAL530:KIX complex using two programs, DAMMIF/N (Fig. 6, B–D) and GASBOR (not shown), provided within the ATSAS package. The models obtained from both methods reasonably fit the experimental data (Table 2 and Fig. S6 (D–F)). Next, we overlaid the DAMMIF/N models of BMAL530 and KIX onto the envelope calculated for the BMAL530:KIX complex (Fig. 6E) (correlation values 0.84 and 0.91 for BMAL530 and KIX, respectively). The KIX domain is positioned in a bulkier region in the bottom part of the BMAL530:KIX complex envelope, and the additional, more elongated density emerging on the top is attributed to BMAL1 regions not directly interacting with the KIX domain.

To further investigate the BMAL1 region extending out of the BMAL1:KIX core complex, we also calculated SAXS models for the complexes of the KIX domain with the longer BMAL517 and BMAL490 constructs using DAMMIF/N (Fig. 7B) and GASBOR (not shown), which showed a good fit to the experimental SAXS data (Fig. S7 (C and D) and Table 2). By comparing the SAXS models of the BMAL530:KIX, BMAL517:KIX, and BMAL490:KIX complexes, we found that the longer BMAL1:KIX complexes are indeed more elongated in shape

**Table 1**

CD measurements suggest that KIX binding does not induce extended regular secondary structures in BMAL1

Spectra were deconvoluted using the CONTIN algorithm with reference data set 6 (46) in the DichroWeb server (45).

	Helix <sup>a</sup>	Strand <sup>a</sup>	Turns	Unordered	NRMSD <sup>b</sup>
BMAL530	0.083	0.104	0.111	0.702	0.032
KIX	0.579	0.062	0.182	0.177	0.016
BMAL530:KIX complex 0 min <sup>c</sup>	0.374	0.036	0.091	0.498	0.075
Complex 30 min <sup>c</sup>	0.363	0.046	0.123	0.468	0.079
Complex ON <sup>c</sup>	0.346	0.081	0.153	0.419	0.064
Calculated for complex <sup>d</sup>	0.311	0.086	0.144	0.460	0.093

<sup>a</sup> Both helices and strands include regular and distorted helices and strands.

<sup>b</sup> Normalized root mean square deviation.

<sup>c</sup> Incubation time after mixing BMAL530 and KIX proteins at time point 0 min, 30 min, and ON (overnight, approximately 17 h).

<sup>d</sup> Deconvolution of averaged CD spectra of individual BMAL530 and KIX proteins.

**Table 2**

SAXS-derived properties of BMAL1, CBP-KIX, and their complexes

See Table S1 for detailed information on SAXS data acquisition and fitting parameters.

Protein	$R_g^a$	$D_{max}^b$	$\chi^2$ (DAMMIF/N, GASBOR)	$MW_t^d$	$MW_E$ (CI) <sup>e</sup>
	$\text{\AA}$	$\text{\AA}$		$kDa$	$kDa$
BMAL530(P624A)	27.7	110	1.14, 1.21	9.7	13.45 (9.95–13.80)
KIX(L664C)	18.9	81	1.26, 1.4	10.32	13.45 (11.65–13.80)
1–10-KIX(L664C)	17.2	64.2	1.21, 1.22	10.68	11.25 (9.95–11.65)
Complex BMAL530(P624A): KIX(L664C)	27.8	114.5	1.06, 1.13	20.02	19.93 (18.35–21.50)
Complex BMAL517:KIX	31.4	137	1.23, 1.36	21.30	21.18 (19.0–23.35)
Complex BMAL490:KIX	37.5	175	1.21, 1.29	24.17	33.10 (29.25–38.10)

<sup>a</sup> Radius of gyration derived from Guinier analysis.

<sup>b</sup> Maximum particle dimension derived from distance distribution function.

<sup>c</sup>  $\chi^2$  values show the best fits of the calculated models with the experimental SAXS data, and the values close to 1 indicate a good fitting.

<sup>d</sup> Theoretical molecular weight based on protein sequence.

<sup>e</sup> Expected molecular weight calculated from a Bayesian inference approach (40) in the ATSAS 2.8.4 software package. CI indicates the credibility interval of molecular weight with 90–98% probability of finding the correct molecular weight in the given range.

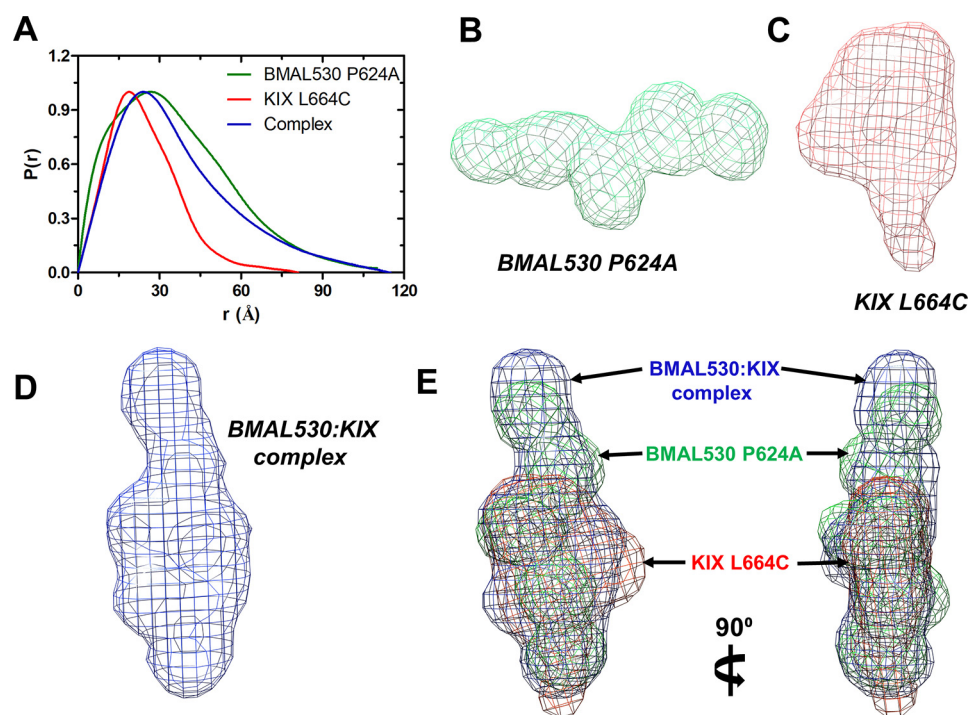


**Figure 6. SAXS analyses of BMAL530, KIX, and the BMAL530:KIX complex.** A, distance distribution functions  $P(r)$  derived from the experimental SAXS data suggest maximum particle dimensions ( $D_{max}$ ) of 110, 81, and 114.5 Å for BMAL530(P624A) (green), KIX(L664C) (red), and their complex (blue), respectively. B–D, *ab initio* SAXS models calculated from DAMMIF/N for BMAL530(P624A) (B), KIX(L664C) (C), and the KIX(L664C):BMAL530(P624A) complex (D). E, the overlay of mesh models of BMAL530(P624A) (green) and KIX(L664C) (red) onto the calculated model of the BMAL530:KIX complex (mesh/blue) positions the KIX domain in the bulkier bottom part of the BMAL530:KIX complex envelope (two views related by 90° rotation). The SAXS envelopes were calculated by DAMMIF/N. The maps were generated from the SAXS envelopes and fitted into each other by Chimera (58).

(Fig. 7C). Notably, all three BMAL1:KIX complex envelopes depict a bulkier region in their bottom part that can be reasonably fit by the KIX domain envelope (Fig. S7 (F–H)) (correlation values 0.91, 0.91, and 0.86 for fitting of the KIX envelope into

BMAL530:KIX, BMAL517:KIX, and BMAL490:KIX complex envelopes, respectively). Furthermore, optimal superposition of the SAXS envelopes of the BMAL530:KIX, BMAL517:KIX, and BMAL490:KIX complexes results in an overlay of their



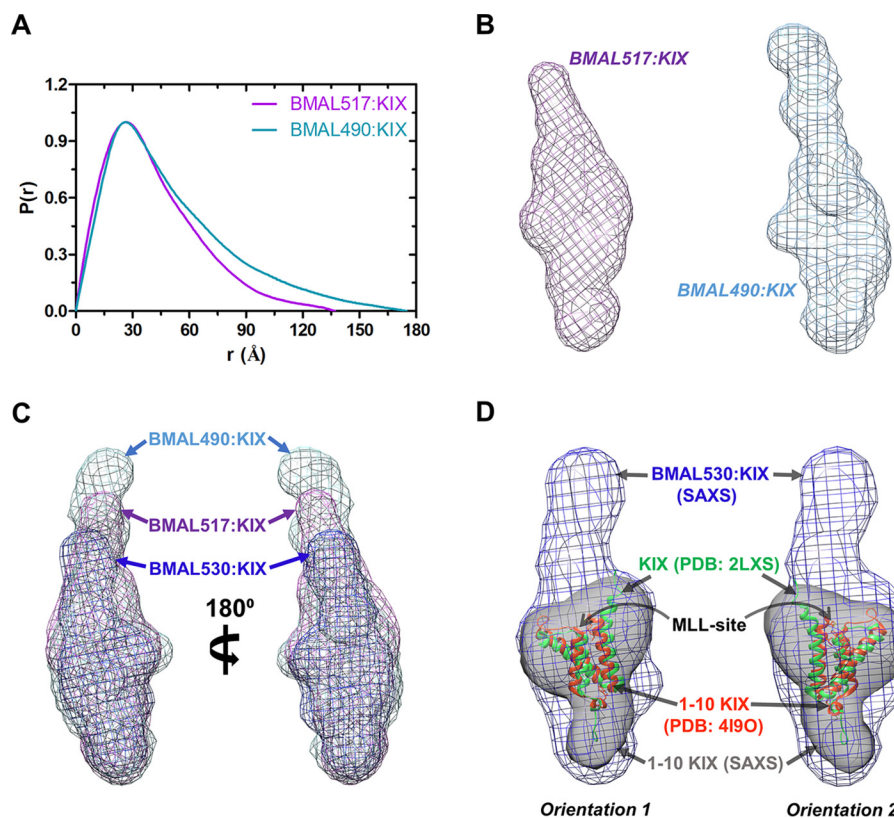


**Figure 7. SAXS analyses of BMAL1:KIX complexes depict N-terminal BMAL1 extensions emerging from the BMAL1-TAD:KIX core complex.** A, distance distribution functions  $P(r)$  derived from the experimental SAXS data result in maximum particle dimensions,  $D_{\max}$ , of 137 and 175 Å for the BMAL517:KIX and BMAL490:KIX complex, respectively. B, *ab initio* SAXS models calculated from DAMMIF/N for the BMAL517:KIX complex (left) and the BMAL490:KIX complex (right). C, superposition of the DAMMIF/N SAXS models (mesh) of the BMAL530(P624A):KIX(L664C) complex (blue), the BMAL517:KIX complex (violet), and the BMAL490:KIX complex (cyan) resulted in an overlay of the bulkier lower parts that accommodate the KIX domain and the KIX-binding C-terminal BMAL1-TAD regions. The gradual elongations at the top of the complex envelopes are consistent with increasing N-terminal extensions of BMAL517 and BMAL490 preceding the BMAL1-TAD. D, the NMR structure of the KIX domain (green, PDB entry 2LXS after SREFLEX) and the 1–10-KIX(L664C) crystal structure (red, PDB entry 4I9O) were fitted into the SAXS envelope of 1–10-KIX(L664C) (calculated with DAMMIF/N) using Chimera (58). Fitting the 1–10-KIX(L664C) SAXS envelope, including the high-resolution KIX structures, into the BMAL530:KIX complex envelope reveals the N-terminal BMAL1 extensions, including parts of the G-region emerging from the BMAL1-TAD:KIX core complex near the MLL-site of KIX (two orientations with KIX rotated by 180°).

bulkier KIX domain regions and highlights elongated extensions of the complex envelopes on one side of the bulkier region that are significantly longer in BMAL490 than in BMAL530 (Fig. 7C). As the C-terminal BMAL1-TAD residues are known to interact with the KIX domain (9), we assigned the narrow-shaped extensions to BMAL1 regions N-terminal to the TAD that do not interact with KIX. Hence, our models identify the location and orientation of the N-terminal ends of the three BMAL1 constructs that emerge from the BMAL1-TAD:CBP-KIX core complex, including the C-terminal BMAL1 residues.

To assess on which side of the KIX domain the N-terminal parts of BMAL1 emerge from the KIX:BMAL1-TAD core complex, we positioned high-resolution three-dimensional structures of the KIX domain in the SAXS envelope of 1–10-tethered KIX. The V-shape of the SAXS models as well as the radius of gyration that we obtained for the 1–10-tethered and untethered KIX(L664C) domain from our experimental SAXS data (Fig. S5, Fig. 6C, and Table 2) are in close agreement with the 1–10-KIX crystal structure (PDB entry 4I9O). However, fitting the theoretical scattering data calculated from the 1–10-KIX crystal structure to the experimental SAXS data resulted in overall unsatisfactory fitting values ( $\chi^2 = 4.73$  (CRY SOL) and  $\chi^2 = 9.24$  (FoXS)) (Fig. S5D). Modeling of N- and C-terminal

residues (Gly<sup>586</sup>, Val<sup>587</sup>, Glu<sup>666</sup>–Leu<sup>672</sup>) that were not included in the 1–10-KIX crystal structure, due to conformational disorder, resulted in a much better fit of the experimental SAXS data ( $\chi^2 = 1.51$  (CRY SOL) and  $\chi^2 = 1.49$  (FoXS); Fig. S5 (E and F)). As these residues are included in the NMR structure of the MLL1:KIX complex (PDB entry 2LXS) and, furthermore, the MLL pocket binds the 1–10 compound (27) and is important for BMAL1 interactions (this study), we also used the MLL1:KIX complex structure to position the KIX domain in the 1–10-KIX SAXS envelope (Fig. 7D). The theoretical scattering profile obtained from the NMR structure of KIX (PDB entry 2LXS, eliminating the MLL1 peptide) fits well to the experimental SAXS profile of 1–10-KIX ( $\chi^2 = 1.57$  after CRY SOL), and the fitting was further improved by model optimization using SREFLEX ( $\chi^2 = 1.21$  after SREFLEX) (Fig. S5E). The fitting of the KIX NMR structure (model obtained after SREFLEX) and of the 1–10-KIX crystal structure to the SAXS envelope of 1–10-tethered KIX and its further superposition onto the SAXS envelope of the BMAL530:KIX complex (Fig. 7D) suggest that the N-terminal BMAL1 region emerges from the KIX domain near the MLL-binding site. By combining our findings with the published literature on BMAL1:KIX interactions (9), we therefore propose that the N-terminal BMAL1 region preceding the

BMAL1-TAD, which includes Lys<sup>537</sup> and parts of the BMAL1 G-region, extends out from the BMAL1-TAD:CBP-KIX core complex near the MLL-binding site with the KIX-binding C-terminal BMAL1-TAD region docked in. We note that based on the low-resolution SAXS envelopes, we cannot entirely exclude alternative orientations of the KIX domain within the bulkier regions of the BMAL1:KIX complex envelopes. However, alternative KIX orientations within the bulkier regions fit the complex shapes less well than the orientation presented in Figs. 6 and 7 and Fig. S7. Moreover, they would result in additional extensions of the SAXS envelopes emerging from the KIX:BMAL1-TAD core complex on the opposite side of the N-terminal BMAL1 regions, which is less consistent with the fact that the most C-terminal BMAL1 residues are engaged in KIX binding (9).

## Discussion

The C-terminal TAD of BMAL1 and the preceding BMAL1 G-region (Glu<sup>429</sup>–Ile<sup>578</sup>), including the acetylated Lys<sup>537</sup>, are of critical functional importance for the mammalian circadian clock (8–13). The BMAL1-TAD facilitates transcriptional repression or activation of CLOCK:BMAL1 by interacting with CRY or the CBP/p300 KIX domain, respectively (9–12, 14, 15). The CBP-KIX domain, on the other hand, interacts with several transcriptional regulators through its MLL- and cMyb/pKID-binding pockets (19). To further our mechanistic understanding of the roles of the BMAL1-TAD-CBP-KIX interaction and its interplay with other KIX ligands and with the BMAL1-CRY interaction in circadian regulation, we investigated the contributions of the MLL- and cMyb/pKID-binding pockets of CBP-KIX, of BMAL1 folding, and of BMAL1 Lys<sup>537</sup> acetylation to the BMAL1-KIX interactions. Our quantitative interaction studies (Figs. 2 and 3) revealed that tethering compound 1–10 to KIX(L664C) or KIX(N627C) in the MLL-binding pocket, which significantly weakens the affinity of the MLL1-TAD to KIX (27), only moderately decreases the affinity of BMAL1 to KIX by about 2-fold. The untethered L664C mutation, which leads to a ~6-fold reduced MLL1-TAD affinity (27), showed a trend of reducing BMAL1 binding affinity. In contrast, the untethered N627C mutation on the opposite side of the MLL-binding pocket showed a trend of enhancing BMAL1 binding. Altogether, these observations suggest that the MLL-binding pocket is involved in BMAL1 interactions, but with a different binding mode of the BMAL1-TAD compared with the MLL1-TAD, possibly in closer proximity to Asn<sup>627</sup>. Diverse binding modes of different ligands in the MLL pocket have been described structurally and are enabled by the intriguing degree of plasticity of the MLL-binding pocket (29).

Interestingly, a 19-mer MLL1-TAD fragment (MLL19) displaces BMAL1 from the prepurified KIX:BMAL530 complex and is only able to pull down KIX, and not BMAL1, when incubated with the individual BMAL530 and KIX proteins (Fig. 2F). The binding site competition between MLL1 and BMAL1 observed in our pulldown experiment further supports the importance of the MLL-binding pocket for BMAL1-TAD interactions. It remains to be investigated how binding site competition between the BMAL1-TAD and the MLL1-TAD for the CBP-KIX domain would impact the acetylation of MLL1 on

Lys<sup>1130</sup> and Lys<sup>1333</sup> by the CBP-HAT domain, which enhances MLL1-dependent H3 Lys<sup>4</sup> trimethylation and subsequent coactivation of CLOCK:BMAL1-dependent circadian genes *in vivo* (32, 33). It is conceivable that recruitment of CBP to the CLOCK:BMAL1 complex requires further stabilization of the BMAL1-CBP interaction (e.g. via additional CBP domains or posttranslational modifications) to enhance specificity of CBP for BMAL1 over alternative KIX-binding transcription factors, such as MLL1. Simultaneous recruitment of CBP and MLL1 to CLOCK:BMAL1 and MLL1 acetylation by CBP would then be possible, as MLL1 interacts with the exon 19 region of CLOCK using a MLL1-binding site near Lys<sup>1130</sup> and Lys<sup>1333</sup> (32, 33), whereas CBP is recruited via BMAL1 (9–12).

To test the role of the second pKID/c-Myb binding pocket in BMAL1 binding, we introduced the mutations Y658A and Y650A/A654W in this pocket, which are known to significantly weaken the interaction of KIX with c-Myb or pKID (21). Interestingly, these mutations only moderately impact BMAL1 binding in our NanoSPR experiments with a ~2–2.5-fold weakened affinity for the Y650A/A654W double mutant and an even less pronounced effect of the Y658A mutant (Fig. 3). The moderate impact of alterations in both KIX-binding pockets on BMAL1 affinity is reminiscent of FOXO3a and suggests that the BMAL1-TAD may, like FOXO3a or p53 (29, 30), interact with both KIX binding sites, but using binding modes different from those used by MLL1, CREB-pKID, or c-Myb. Solution NMR structures showed that FOXO3a binds to both KIX-binding pockets simultaneously with its conserved regions 2 and 3 (CR2C and CR3) adopting two different conformations and orientations that also deviate from the orientations and interactions of the MLL1-TAD or pKID peptides (29). In the case of the p53-TAD, its two subdomains AD1 and AD2 synergistically bind to both KIX-binding sites (30). Like AD1 and AD2 of the p53-TAD, CR2C and CR3 of FOXO3a, and other transactivation domains of KIX-binding proteins, the BMAL1-TAD contains a ΦXXΦΦ motif (LXXLL<sup>606</sup>) (where Φ represents a hydrophobic residue), which could potentially bind to either of the two KIX-binding sites. Mutational studies showed that the LXXLL<sup>606</sup> motif of BMAL1 is much more important for KIX binding than the seven most C-terminal BMAL1 residues, as the L605A/L606A double mutation completely disrupts the BMAL1-KIX interaction, whereas deletion of the C-terminal BMAL1 residues only leads to a 2-fold reduced affinity (9). As the MLL19-TAD peptide completely displaces BMAL1 (Fig. 2F), we presently favor a scenario in which the more important BMAL1 interaction site is located near the MLL-binding pocket.

Consistent with previous studies (9, 14), our CD and SAXS analyses showed that the BMAL1-TAD and the preceding N-terminal regions are intrinsically disordered (Table 1, Fig. 5A, and Fig. S6B), allowing the BMAL1-TAD to dynamically interact with co-regulators in the mammalian circadian clock. The BMAL1-TAD undergoes conformational rearrangements upon binding to CRY1 and KIX, as suggested by manganese-dependent paramagnetic relaxation enhancement studies (9), which prompted us to further biophysically characterize the formation of the BMAL1-TAD:KIX complex by CD spectroscopy. Interestingly, BMAL1-TAD binding to the KIX domain does not lead to pronounced changes in secondary structure



content compared with averaged spectra of BMAL530 and KIX proteins (Table 1 and Fig. 5B). Therefore, our CD spectra do not suggest major folding events of extended unstructured BMAL1 regions upon KIX binding, such as the induced folding of the CREB-pKID and cMyb-TAD (20, 23). However, the CD data do not exclude conformational rearrangements associated with minor secondary structure changes (e.g. a locally enhanced helical folding of the IXXLL<sup>606</sup> motif region at the KIX interface or orientation changes of the polypeptide chain).

SAXS analyses of the BMAL530 fragment revealed that the BMAL1-TAD and the included parts of the G-region are elongated, lacking a compact domain and mostly unfolded (Fig. 6, Fig. S6, and Table 2). Furthermore, the extended shape of the BMAL530:KIX complex with a  $D_{\max}$  similar to unbound BMAL530 and the Kratky plot analyses together suggest that the BMAL1-TAD does not fold upon KIX binding (Fig. 6, Fig. S6, and Table 2), consistent with our CD spectra (Fig. 5 and Table 1). The comparison and superposition of the BMAL530:KIX complex with the complexes including longer BMAL1 fragments (BMAL517:KIX and BMAL490:KIX) revealed that parts of the BMAL1 fragments extend out of the bulkier BMAL1-TAD:KIX core complex (Fig. 7, Fig. S7, and Table 2). Based on KIX-BMAL1 interaction studies reported previously (9) and presented herein as well as the fitting of the SAXS envelope and high-resolution three-dimensional structures of the KIX domain into our SAXS models of the three BMAL1:KIX complexes (Fig. 7D and Fig. S7 (F–H)), we propose that the C-terminal BMAL1-TAD region is bound to the KIX domain utilizing both binding sites, whereas the N-terminal part preceding the BMAL1-TAD and including parts of the G-region emerges from the KIX:BMAL1-TAD core complex near the MLL-binding pocket. This model interpretation is also consistent with our finding that the MLL1-TAD interferes with BMAL1-TAD:KIX complex formation (Fig. 2F). Whereas high-resolution structure determination studies are still required to look closely into the structure of the complex, our model provides a plausible starting point to further mechanistically probe BMAL1-CBP interactions.

Using NanoSPR and MST measurements, we found that the K537Q mutation does not affect the affinity of BMAL530 for KIX (Fig. 4). This finding contrasts with the enhancing effect of both the *in vitro* K537Q mutation (14, 15) and the *in vivo* Lys<sup>537</sup> acetylation (13) on CRY1 binding. Assuming that the K537Q mutation mimics the effect of Lys<sup>537</sup> acetylation on CBP-KIX-BMAL1-TAD interactions as well as that reported for CRY1-BMAL1-TAD interactions (13–15), our result suggests that Lys<sup>537</sup> acetylation does not affect the BMAL1-TAD-CBP-KIX interaction. However, in the context of full-length CBP and in cells, Lys<sup>537</sup> acetylation could still modulate BMAL1-CBP interactions by alternative mechanisms, as for example in the case of acetylated CREB-pKID (41), and the putative effect of BMAL1 Lys<sup>537</sup> acetylation on CBP-dependent co-activation of CLOCK:BMAL1 or circadian chromatin modification remains to be investigated *in vivo*.

Unexpectedly, we observed overall lower KIX-binding affinities of BMAL530 in our MST and FP experiments (Fig. 2) compared with our NanoSPR experiments (Fig. 3) and published data (16), which we attribute to the N-terminal fusion of

BMAL530 to a fluorescently labeled hexahistidine tag. Therefore, modifications of the BMAL1 region N-terminal to the TAD could have an impact on the BMAL1-TAD-KIX interaction. This finding may be correlated with the documented functional importance of the BMAL1 G-region (9).

Overall, this study has highlighted the significance of the MLL-binding pocket of KIX for BMAL1 interactions and determined the location of the N-terminal regions of our BMAL1 constructs, including parts of the G-region, with respect to the BMAL1-TAD:KIX core complex. Additionally, we observed a moderate effect of mutants in the second KIX-binding pocket, suggesting that it also affects BMAL1 binding. However, our results showed that the second KIX-binding pocket does not play a predominant role for BMAL1 binding, and BMAL1 does not bind to KIX in a CREB-pKID-like manner, in which case a positive cooperative effect of MLL1-TAD binding and 1–10 tethering to Asn<sup>627</sup> might be expected as for pKID (26, 28), rather than the negative interference that we observed (Figs. 2 and 3). Based on the presented data, formation of a ternary complex between BMAL1, CBP, and CREB cannot, therefore, be excluded. The interplay between BMAL1 and CREB binding to CBP should be further investigated, as it plays a critical role in defining recruitment of CBP to CLOCK:BMAL1 and/or CREB to regulate circadian transcription and chromatin modification as well as phase resetting and light entrainment of the clock via *per1* gene activation (34, 35). Thereby, the impact of additional CBP domains also needs to be taken into account as well as posttranslational modifications of pKID and BMAL1, such as CREB-pKID phosphorylation on Ser<sup>133</sup> and Ser<sup>142</sup>, which affects KIX binding and plays a critical role in suprachiasmatic nucleus light entrainment (34). Altogether, our study has significantly advanced our mechanistic understanding of CBP-BMAL1 interactions and lays a stepping stone for further structural and mechanistic analyses of the protein interaction network underlying CBP-dependent gene regulation in the mammalian circadian clock.

## Experimental procedures

### Cloning, mutagenesis, expression, and purification of BMAL1 and KIX proteins

The mouse CBP KIX domain (residues 586–672) was subcloned from full-length mouse CBP (pcDNA3β-FLAG-CBP-HA; Addgene). The C-terminal mouse BMAL1-(530–625) (BMAL530) and BMAL1(517–625) (BMAL517) constructs were subcloned from the BMAL1(490–625) (BMAL490) template (14). The CBP-KIX and BMAL1 constructs were subcloned into pCoofy1 with an N-terminal His<sub>6</sub> tag and a 3C PreScission protease site for removal of the tag using ligation-independent cloning (42). The mutations were introduced into the BMAL530 and KIX constructs using a modified QuikChange method (43).

The KIX domain and the BMAL1 proteins (BMAL530/517/490) were overexpressed in the *Escherichia coli* Rosetta (DE3) strain, induced with 0.5 mM isopropyl β-D-1-thiogalactopyranoside at an OD<sub>600</sub> of ~0.8, and cooled down to 25 °C or 30 °C for 4–5 h. For purification, 2–4 liters of cells overexpressing BMAL1 or KIX proteins were grown in Terrific broth medium



and resuspended homogenously in lysis buffer containing 50 mM Tris-Cl, pH 7.2, 250 mM NaCl, 5 mM 2-mercaptoethanol, and 10% glycerol. Prior to lysis, 1 mM phenylmethylsulfonyl fluoride and benzonase were added, and the cells were lysed in a fluidizer. The supernatant after the centrifugation was loaded on a  $\text{Ni}^{2+}$  affinity column (GE Healthcare), and the protein was eluted with a linear gradient of 0–500 mM imidazole. The tag was cleaved using His-PreScission protease and dialyzed against a buffer containing no imidazole using a 3-kDa cutoff Roth ZelluTrans dialysis membrane. The cleaved proteins were further cleaned up using a second  $\text{Ni}^{2+}$  affinity column for trapping the protease and the tag before loading on a Superdex S75 16/60 column (GE Healthcare). The KIX mutants were purified using the same procedure. The His<sub>6</sub>-tagged BMAL530(K537Q) mutant was expressed at 18 °C overnight after induction with 0.5 mM isopropyl  $\beta$ -D-1-thiogalactopyranoside and purified as described for WT BMAL1. For the purification of BMAL530(P624A), the protein was further cleaned up using a Q HP anion-exchange column (GE Healthcare) before loading it on a Superdex S75 16/60 column (GE Healthcare). The identity of the proteins was confirmed by MS. The theoretical molecular weights calculated for BMAL1 and KIX proteins are BMAL530 (9.72 kDa), BMAL517 (10.97 kDa), BMAL490 (13.84 kDa), and KIX (10.33 kDa). The BMAL530:KIX, BMAL517:KIX, and BMAL490:KIX complexes were purified by co-lysis of cells overexpressing the individual BMAL530, BMAL517, or BMAL490 proteins for the respective complexes with cells overexpressing the KIX protein. The remaining purification procedure was followed as for the individual BMAL1 and KIX proteins.

#### Limited proteolysis of the BMAL490:KIX complex

The limited proteolysis experiments were performed by mixing a 40- $\mu$ l protein solution of 1 mg/ml BMAL490:KIX complex with 12  $\mu$ l of 0.1 mg/ml sequencing-grade GluC protease solution. The reactions were incubated for 30 and 60 min. The protease activity was stopped by boiling for 10 min with 5x SDS protein-loading buffer, and the cleavage products were resolved by SDS-PAGE. The N- and C-terminal construct boundaries were determined by performing an in-gel acid hydrolysis using 3 M HCl followed by a peptide cleanup and MS using an LC-MS/MS system (LTQ Orbitrap Velos Pro, Thermo Fisher Scientific).

#### Synthesis of compound 1–10 (27)

Tris-(2-ethylcarboxy)phosphine hydrochloride (19.5 mg, 0.068 mmol) was added to a solution of bis(2-dimethylaminoethyl) disulfide dihydrochloride (959 mg, 3.41 mmol) in dimethylformamide (30 ml) and water (3 ml). 3,3'-Disulfanediybis(1-(4-(4-chloro-3-(trifluoromethyl)phenyl)-4-hydroxypiperidin-1-yl)propan-1-one) (500 mg, 0.68 mmol) and triethylamine (2 ml) were then added, and the reaction mixture was stirred overnight at room temperature. The reaction was concentrated *in vacuo* to remove dimethylformamide, and the residue was dissolved in dichloromethane (30 ml) and washed three times with brine (30 ml). The organic layer was dried over  $\text{Na}_2\text{SO}_4$  and concentrated *in vacuo*. The crude residue was purified by column chromatography (MeOH/dichloromethane: 2:98 to 10:90) yielding a yellowish-white solid (205 mg, 64%). Structure, purity, and mass were confirmed by proton and carbon NMR, LC-MS, and MS. ( $[\text{M} + \text{H}]^+$  calculated 471.11, found 471.15).

#### Tethering of KIX(L664C) and KIX(N627C) with compound 1–10

For affinity measurements by NanoSPR, FP, and MST, the purified KIX(L664C) and KIX(N627C) proteins were tethered with compound 1–10 following the published protocol (27). Briefly, the protein was buffer-exchanged into sodium phosphate buffer, pH 6.8, using a 5-ml HiTrap desalting column (GE Healthcare), tethered with a 10-fold molar excess of compound 1–10, and then further buffer-exchanged to 25 mM HEPES buffer, pH 7.2, 100 mM NaCl, and 0.05% Tween 20.

#### Confirmation of complete 1–10 compound incorporation by MS

Samples were diluted 10-fold with 30% acetonitrile (LC-MS grade, Roth) and analyzed by direct infusion MS on a Synapt G2-S HDMS mass spectrometer (Waters Corp.). The TOF analyzer of the mass spectrometer was externally calibrated with a sodium formate mixture from  $m/z$  50 to 1990. Spectra were acquired at 25,000 resolution (FWHM) using a 1-s scan time. Mass spectrometric raw data were analyzed manually using MassLynx version 4.1 software (Waters Corp.).

#### Microscale thermophoresis

The MST measurements were performed in standard treated capillaries on a NanoTemper Monolith NT.115 instrument. The measurements were done following the manual instructions at 90% LED (based on the initial fluorescence intensity) and 60% MST power (IR laser power) with a 30-s laser-on time and 5-s laser-off time. The purified N-terminally His<sub>6</sub>-tagged BMAL530(P624A) protein was labeled with RED-tris-NTA NT-647 dye (Nanotemper Technologies) following the recommended protocol in a buffer containing 25 mM HEPES, pH 7.2, 100 mM NaCl, and 0.05% Tween 20. Briefly, a 200 nM His<sub>6</sub>-BMAL1 protein solution was mixed in a 1:1 ratio (v/v) with a 100 nM RED-tris-NTA dye solution and incubated for 30 min at room temperature. The excess dye was removed by centrifugation at  $15,000 \times g$  for 10 min. The unlabeled and untagged KIX domain (WT and mutants) was titrated in the final concentration range of 160 to 0.005  $\mu\text{M}$ , mixed in a 1:1 ratio (v/v) with the labeled BMAL1 protein, thereby keeping the final BMAL1 concentration at 50 nM, and filled in the standard capillaries for measurement after incubating for 30 min at room temperature. The normalized fluorescence values were plotted against the untagged protein (titrant) concentration. The data were analyzed using a one-site binding model in GraphPad Prism to obtain the  $K_D$  values.

#### Fluorescence polarization

For FP measurements, the purified N-terminally His<sub>6</sub>-tagged BMAL530(P624A) protein was labeled with the RED-tris-NTA NT-647 fluorescent dye (Nanotemper Technologies). The labeling reaction was performed similarly to the MST experiments in a buffer containing 25 mM HEPES, pH 7.2, 100 mM NaCl, and 0.05% Tween 20. Unlabeled proteins (KIX WT/mutants) were titrated in the final concentration range of 0.04–80  $\mu\text{M}$ , thereby keeping the concentration of labeled BMAL1 molecules constant at 50 nM. The reactions were incubated for 30 min at room temperature and transferred to a

384-well Corning flat black low-volume plate. The measurements were carried out with a Tecan Spark 20M plate reader in polarization mode at 25 °C using excitation and emission wavelengths for the NT-647 dye at 625 and 665 nm, respectively. The dissociation constants were obtained by fitting the concentration-dependent change in polarization using a nonlinear regression function and a one-site specific fit in GraphPad Prism.

## Preparation, characterization, and functionalization of gold nanorod particles for NanoSPR

Cetyl trimethylammonium bromide-stabilized gold nanorods were synthesized as described previously (37). Two batches of nanoparticles were prepared that had bulk resonance wavelengths ( $\lambda_{\text{res}}$ ) centered at 650 nm (batch 1) and 730 nm (batch 2), respectively. Particles from batch 1 had a diameter of  $27.2 \pm 3.2$  nm and a length of  $65.4 \pm 4.7$  nm, whereas particles from batch 2 had a diameter of  $33.2 \pm 3.7$  nm and a length of  $91.4 \pm 7.0$  nm, as determined by transmission EM. Both particle batches led to similar signal/noise ratios, and their application in NanoSPR experiments resulted in similar  $K_D$  values. To enable binding to the His-tagged protein receptors, the cetyl trimethylammonium bromide layer around the particles was replaced by NTA, and the His tags of the receptor proteins were complexed with nickel, adapting an established protocol (38).

For the NanoSPR measurements, the prepared NTA particles were divided into small batches. Each batch was independently functionalized in solution with a different Ni-His<sub>6</sub>-tagged protein receptor (*i.e.* with Ni-His<sub>6</sub>-BMAL530 WT or mutants (BMAL530(K537Q) or BMAL530(P624A))) for interaction with the untagged KIX domain or with Ni-His<sub>6</sub>-KIX WT or mutants (untethered/1–10-tethered KIX(L664C), untethered/1–10-tethered KIX(N627C), KIX(Y658A), or KIX(Y650A/A654W) double mutant) for the interaction with untagged BMAL530(P624A), thus making a library of nanoparticle-protein receptor conjugates. Functionalization was carried out by co-incubating NTA particles with Ni-His<sub>6</sub>-tagged proteins for 5 min at room temperature in buffer containing 25 mM HEPES, pH 7.2, 100 mM NaCl, and 5% glycerol.

## Single-nanoparticle plasmon spectroscopy and NanoSPR

We flushed and sequentially immobilized the different batches of functionalized nanoparticle receptor conjugates in the microfluidic flow cell and recorded the position of every single nanosensor as described (37) to create a position-encoded sensor substrate. Before and after each particle deposition step, we washed the flow cell generously with buffer (25 mM HEPES, pH 7.2, 100 mM NaCl, 5% glycerol) to remove unbound particles and proteins.

The optical dark-field spectroscopy setup used to record single-particle spectra was described in detail recently (36, 44). Each nanoparticle receptor sensor has a characteristic plasmon resonance wavelength ( $\lambda_{\text{res}}$ ), which will have a spectral shift ( $\Delta\lambda_{\text{res}}$ ) upon binding of biomolecules near the nanoparticle surface (37). To obtain satisfactory statistics of the responses over many sensors, we used a spectral imaging detection method that allowed for the investigation of all of the particles within the field of view simultaneously as described (36, 44).

To carry out a titration experiment, 100  $\mu\text{l}$  of a ligand solution (untagged KIX or BMAL530(P624A) proteins) with a given concentration was flushed into the flow cell at a flow rate of 50  $\mu\text{l}/\text{min}$ , and the spectral shift ( $\Delta\lambda_{\text{res}}$ ) of every particle (80–200 particles for each protein receptor) was recorded with a time resolution of about 1 min at this ligand concentration until an equilibrium value ( $\Delta\lambda_{\text{max}}$ ) was reached. This process was repeated for 8–10 different ligand concentrations (0.045–25  $\mu\text{M}$ ). To determine the binding parameters, the following equation was used,

$$\Delta\lambda/\Delta\lambda_{\text{max}} = [\text{ligand}]/K_D + [\text{ligand}] \quad (\text{Eq. 1})$$

(with the coverage  $\Theta = \Delta\lambda/\Delta\lambda_{\text{max}}$ ) as fitting function, and the dissociation constants were obtained using a one-site binding model in GraphPad Prism by plotting the normalized wavelength shifts as a function of ligand concentration.

## GST pulldown

The His<sub>6</sub>GST-tagged human MLL1-TAD peptide (denoted as MLL19) comprising residues <sup>2840</sup>DCGNILPSDIMDFV-LKNT<sup>2858</sup> (equivalent to Asp<sup>2836</sup>–Pro<sup>2854</sup> with identical sequence in mouse MLL1) was subcloned from full-length human MLL1 (in pTARGET<sup>TM</sup>) into pCoofy3, expressed in *E. coli*, and purified using Ni<sup>2+</sup>-affinity and size-exclusion chromatography in a buffer containing 25 mM HEPES, pH 7.2, 150 mM NaCl, 5% glycerol, and 2 mM DTT. A concentration of 4  $\mu\text{M}$  GST-tagged MLL19 (bait), 20  $\mu\text{M}$  BMAL530:KIX complex, or individual BMAL530 and KIX proteins (prey) and ~20  $\mu\text{l}$  of GSH agarose (Sigma) was used for pulldown in a reaction volume of 200  $\mu\text{l}$ . The reactions were washed three times with the above buffer following the overnight rotation at 4 °C. The protein was eluted with SDS protein-loading buffer and boiled for ~5 min followed by SDS-PAGE.

## CD spectroscopy

CD spectra were recorded with a Jasco-815 spectropolarimeter using a quartz cuvette of 0.1-cm pathlength. The measurements were performed in continuous scan mode with accumulation of six scans for each measurement at 4 °C for BMAL530 and KIX (WT and mutants) and at 20 °C for the complexes. The data were collected at every nm from 185 to 250 nm at a scan speed of 50 nm/min. The purified proteins were diluted to a final concentration of 10–20  $\mu\text{M}$  in 20 mM sodium phosphate buffer, pH 7.2. The CD spectra from individual BMAL530 and KIX proteins were averaged for the calculated spectra of the complex. The machine units (in millidegrees,  $\theta$ ) were converted to mean residue ellipticity ( $MRE$ ,  $[\theta]_R$ ) from mean residue weight ( $MRW$ ), path length ( $l$ , in cm), and protein concentration ( $c$ , in mg/ml) using the following equation.

$$MRE = \theta \times (0.1 \times MRW)/lc \quad (\text{Eq. 2})$$

The data were deconvoluted, and the protein secondary structure was calculated using the CONTIN algorithm in the DichroWeb server (45) with the reference data set 6 (46).

## SAXS

The data were collected on the SAXS beamline P12 (47) at PETRA III, DESY, Hamburg with an X-ray wavelength of 1.24



Å. The measurements of protein solutions were carried out in the concentration range of 0.1–11 mg/ml to check for the interference between protein molecules at different concentrations and to obtain high-quality data. The PRIMUS Qt program in the ATSAS 2.8.4 software package (48) was used for processing the data, and from small  $q$ -regions of the scattering data, the radius of gyration ( $R_g$ ) was determined using the Guinier approximation. The molecular weights were determined using a Bayesian inference approach (40) implemented in the ATSAS 2.8.4. software. The pairwise-distribution function ( $P(r)$ ) was computed using GNOM (49), which gives the maximum dimension ( $D_{\max}$ ) of the macromolecule. The GNOM output file was used by the *ab initio* shape-determination programs GASBOR (50) and DAMMIF (51), which generated 10 independent low-resolution envelopes that were averaged together using DAMAVER (52) and refined using DAMMIN (53).

The programs FoXS (54) and CRY SOL (55) were used to calculate the theoretical scattering profiles from published KIX structures (PDB entries 4I9O and 2LXS) and for fitting them to the experimental SAXS data. The SREFLEX program (56) was used to further improve the agreement of the NMR structure of the KIX domain (from PDB entry 2LXS, eliminating MLL1 peptide) to the experimental SAXS data calculated for 1–10-KIX by estimating flexibility of the high-resolution structure. To improve the fit of the 1–10-KIX crystal structure to the SAXS envelope, residues Gly<sup>586</sup>, Val<sup>587</sup>, and Glu<sup>666</sup>–Leu<sup>672</sup>, which were missing in the crystal structure of 1–10 KIX(L664C) (PDB entry 4I9O), were modeled using MODELLER version 9.20 (57). The program Chimera (58) was used for the conversion of SAXS envelopes into maps (command: molmap) and to superpose the maps of the KIX:BMAL530, KIX:BMAL517, and KIX:BMAL490 complexes onto each other (tool: “Fit in Map”). The Fit in Map option of Chimera was also used to fit the SAXS envelopes obtained for KIX and BMAL530 into the SAXS envelope of the BMAL530:KIX complex and to fit the KIX structures into the SAXS map of 1–10-KIX.

## Data accession

The SAXS scattering data collected at the P12 beamline has been deposited in the Small Angle Scattering Biological Data Bank (SASBDB) (59) with the following accession codes: BMAL1(530–625)P624A (SASDF27), KIX(L664C) (SASDF37), BMAL530(P624A):KIX(L664C) complex (SASDF47), BMAL517:KIX complex (SASDF57), BMAL490:KIX complex (SASDF67), and 1–10-tethered KIX (SASDF77).

**Author contributions**—A. G. and E. W. conceptualization; A. G., W. Y., and U. D. formal analysis; A. G., W. Y., U. D., and E. W. validation; A. G., R. O., W. Y., U. D., and J. E. C. investigation; A. G., U. D., and E. W. visualization; A. G., R. O., W. Y., U. D., and J. E. C. methodology; A. G. and E. W. writing-original draft; A. G. and E. W. project administration; A. G. and E. W. writing-review and editing; M. K., S. T., C. S., and E. W. resources; M. K., S. T., C. S., and E. W. supervision; E. W. funding acquisition; R. O. performed SAXS experiments; W. Y. performed and analyzed nanoSPR experiments; U. D. mass spectrometry to analyze 1–10 compound incorporation; J. E. C. 1–10 compound synthesis.

**Acknowledgments**—We thank the Proteomics Core Facilities of the IMB Mainz and EMBL Heidelberg for mass spectrometric measurements as well as the Core Facilities Media laboratory and protein production (IMB Mainz) for continuous support. We also thank Dr. Rubén Ahijado-Guzmán for discussions and help with NanoSPR measurements, Benedict Junglas for help with CD measurements, and Dr. Nadja Hellmann and Dr. Elmar Jaenicke for thoughtful discussions. Furthermore, we thank Dr. Nelly Hajizadeh for assistance during SAXS data collection at the P12 beamline, DESY Hamburg. The full-length MLL1 plasmid was a generous gift from Prof. Rolf Marschalek.

## References

- Merbitz-Zahradnik, T., and Wolf, E. (2015) How is the inner circadian clock controlled by interactive clock proteins?: structural analysis of clock proteins elucidates their physiological role. *FEBS Lett.* **589**, 1516–1529 [CrossRef Medline](#)
- Partch, C. L., Green, C. B., and Takahashi, J. S. (2014) Molecular architecture of the mammalian circadian clock. *Trends Cell Biol.* **24**, 90–99 [CrossRef Medline](#)
- Koike, N., Yoo, S.-H., Huang, H.-C., Kumar, V., Lee, C., Kim, T.-K., and Takahashi, J. S. (2012) Transcriptional architecture and chromatin landscape of the core circadian clock in mammals. *Science* **338**, 349–354 [CrossRef Medline](#)
- Aryal, R. P., Kwak, P. B., Tamayo, A. G., Gebert, M., Chiu, P.-L., Walz, T., and Weitz, C. J. (2017) Macromolecular assemblies of the mammalian circadian clock. *Mol. Cell* **67**, 770–782.e6 [CrossRef Medline](#)
- Ye, R., Selby, C. P., Ozturk, N., Annayev, Y., and Sancar, A. (2011) Biochemical analysis of the canonical model for the mammalian circadian clock. *J. Biol. Chem.* **286**, 25891–25902 [CrossRef Medline](#)
- Ye, R., Selby, C. P., Chiou, Y.-Y., Ozkan-Dagliyan, I., Gaddameedhi, S., and Sancar, A. (2014) Dual modes of CLOCK:BMAL1 inhibition mediated by Cryptochrome and Period proteins in the mammalian circadian clock. *Genes Dev.* **28**, 1989–1998 [CrossRef Medline](#)
- Etchegaray, J.-P., Lee, C., Wade, P. A., and Reppert, S. M. (2003) Rhythmic histone acetylation underlies transcription in the mammalian circadian clock. *Nature* **421**, 177–182 [CrossRef Medline](#)
- Bunger, M. K., Wilsbacher, L. D., Moran, S. M., Clendenen, C., Radcliffe, L. A., Hogenesch, J. B., Simon, M. C., Takahashi, J. S., and Bradfield, C. A. (2000) Mop3 is an essential component of the master circadian pacemaker in mammals. *Cell* **103**, 1009–1017 [CrossRef Medline](#)
- Xu, H., Gustafson, C. L., Sammons, P. J., Khan, S. K., Parsley, N. C., Ramanathan, C., Lee, H.-W., Liu, A. C., and Partch, C. L. (2015) Cryptochrome 1 regulates the circadian clock through dynamic interactions with the BMAL1 C terminus. *Nat. Struct. Mol. Biol.* **22**, 476–484 [CrossRef Medline](#)
- Park, N., Kim, H.-D., Cheon, S., Row, H., Lee, J., Han, D.-H., Cho, S., and Kim, K. (2015) A novel Bmal1 mutant mouse reveals essential roles of the C-terminal domain on circadian rhythms. *PLoS One* **10**, e0138661 [CrossRef Medline](#)
- Takahata, S., Ozaki, T., Mimura, J., Kikuchi, Y., Sogawa, K., and Fujii-Kuriyama, Y. (2000) Transactivation mechanisms of mouse clock transcription factors, mClock and mArnt3. *Genes Cells* **5**, 739–747 [CrossRef Medline](#)
- Kiyohara, Y. B., Tagao, S., Tamanini, F., Morita, A., Sugisawa, Y., Yasuda, M., Yamanaka, I., Ueda, H. R., van der Horst, G. T. J., Kondo, T., and Yagita, K. (2006) The BMAL1 C terminus regulates the circadian transcription feedback loop. *Proc. Natl. Acad. Sci. U.S.A.* **103**, 10074–10079 [CrossRef Medline](#)
- Hirayama, J., Sahar, S., Grimaldi, B., Tamaru, T., Takamatsu, K., Nakahata, Y., and Sassone-Corsi, P. (2007) CLOCK-mediated acetylation of BMAL1 controls circadian function. *Nature* **450**, 1086–1090 [CrossRef Medline](#)
- Czarna, A., Breitkreuz, H., Mahrenholz, C. C., Arens, J., Strauss, H. M., and Wolf, E. (2011) Quantitative analyses of cryptochrome-mBMAL1 interactions: mechanistic insights into the transcriptional regulation of the



- mammalian circadian clock. *J. Biol. Chem.* **286**, 22414–22425 [CrossRef](#) [Medline](#)
15. Czarna, A., Berndt, A., Singh, H. R., Grudziecki, A., Ladurner, A. G., Timinszky, G., Kramer, A., and Wolf, E. (2013) Structures of *Drosophila* cryptochrome and mouse cryptochrome1 provide insight into circadian function. *Cell* **153**, 1394–1405 [CrossRef](#) [Medline](#)
16. Gustafson, C. L., Parsley, N. C., Asimgil, H., Lee, H.-W., Ahlback, C., Michael, A. K., Xu, H., Williams, O. L., Davis, T. L., Liu, A. C., and Partch, C. L. (2017) A slow conformational switch in the BMAL1 transactivation domain modulates circadian rhythms. *Mol. Cell.* **66**, 447–457.e7 [CrossRef](#) [Medline](#)
17. Vo, N., and Goodman, R. H. (2001) CREB-binding protein and p300 in transcriptional regulation. *J. Biol. Chem.* **276**, 13505–13508 [CrossRef](#) [Medline](#)
18. Dyson, H. J., and Wright, P. E. (2016) Role of intrinsic protein disorder in the function and interactions of the transcriptional coactivators CREB-binding protein (CBP) and p300. *J. Biol. Chem.* **291**, 6714–6722 [CrossRef](#) [Medline](#)
19. Thakur, J. K., Yadav, A., and Yadav, G. (2014) Molecular recognition by the KIX domain and its role in gene regulation. *Nucleic Acids Res.* **42**, 2112–2125 [CrossRef](#) [Medline](#)
20. Radhakrishnan, I., Pérez-Alvarado, G. C., Parker, D., Dyson, H. J., Montminy, M. R., and Wright, P. E. (1997) Solution structure of the KIX domain of CBP bound to the transactivation domain of CREB: a model for activator:coactivator interactions. *Cell* **91**, 741–752 [CrossRef](#) [Medline](#)
21. Parker, D., Rivera, M., Zor, T., Henrion-Caude, A., Radhakrishnan, I., Kumar, A., Shapiro, L. H., Wright, P. E., Montminy, M., and Brindle, P. K. (1999) Role of secondary structure in discrimination between constitutive and inducible activators. *Mol. Cell. Biol.* **19**, 5601–5607 [CrossRef](#) [Medline](#)
22. Zor, T., Mayr, B. M., Dyson, H. J., Montminy, M. R., and Wright, P. E. (2002) Roles of phosphorylation and helix propensity in the binding of the KIX domain of CREB-binding protein by constitutive (c-Myb) and inducible (CREB) activators. *J. Biol. Chem.* **277**, 42241–42248 [CrossRef](#) [Medline](#)
23. Gianni, S., Morrone, A., Giri, R., and Brunori, M. (2012) A folding-after-binding mechanism describes the recognition between the transactivation domain of c-Myb and the KIX domain of the CREB-binding protein. *Biochem. Biophys. Res. Commun.* **428**, 205–209 [CrossRef](#) [Medline](#)
24. De Guzman, R. N., Goto, N. K., Dyson, H. J., and Wright, P. E. (2006) Structural basis for cooperative transcription factor binding to the CBP coactivator. *J. Mol. Biol.* **355**, 1005–1013 [CrossRef](#) [Medline](#)
25. Bruschweiler, S., Konrat, R., and Tollinger, M. (2013) Allosteric communication in the KIX domain proceeds through dynamic repacking of the hydrophobic core. *ACS Chem. Biol.* **8**, 1600–1610 [CrossRef](#) [Medline](#)
26. Goto, N. K., Zor, T., Martinez-Yamout, M., Dyson, H. J., and Wright, P. E. (2002) Cooperativity in transcription factor binding to the coactivator CREB-binding protein (CBP): the mixed lineage leukemia protein (MLL) activation domain binds to an allosteric site on the KIX domain. *J. Biol. Chem.* **277**, 43168–43174 [CrossRef](#) [Medline](#)
27. Wang, N., Majmudar, C. Y., Pomerantz, W. C., Gagnon, J. K., Sadowsky, J. D., Meagher, J. L., Johnson, T. K., Stuckey, J. A., Brooks, C. L., 3rd, Wells, J. A., and Mapp, A. K. (2013) Ordering a dynamic protein via a small-molecule stabilizer. *J. Am. Chem. Soc.* **135**, 3363–3366 [CrossRef](#) [Medline](#)
28. Wang, N., Lodge, J. M., Fierke, C. A., and Mapp, A. K. (2014) Dissecting allosteric effects of activator-coactivator complexes using a covalent small molecule ligand. *Proc. Natl. Acad. Sci. U.S.A.* **111**, 12061–12066 [CrossRef](#) [Medline](#)
29. Wang, F., Marshall, C. B., Yamamoto, K., Li, G.-Y., Gasmi-Seabrook, G. M. C., Okada, H., Mak, T. W., and Ikura, M. (2012) Structures of KIX domain of CBP in complex with two FOXO3a transactivation domains reveal promiscuity and plasticity in coactivator recruitment. *Proc. Natl. Acad. Sci. U.S.A.* **109**, 6078–6083 [CrossRef](#) [Medline](#)
30. Lee, C. W., Arai, M., Martinez-Yamout, M. A., Dyson, H. J., and Wright, P. E. (2009) Mapping the interactions of the p53 transactivation domain with the KIX domain of CBP. *Biochemistry* **48**, 2115–2124 [CrossRef](#) [Medline](#)
31. Lee, B., Li, A., Hansen, K. F., Cao, R., Yoon, J. H., and Obrietan, K. (2010) CREB influences timing and entrainment of the SCN circadian clock. *J. Biol. Rhythms* **25**, 410–420 [CrossRef](#) [Medline](#)
32. Katada, S., and Sassone-Corsi, P. (2010) The histone methyltransferase MLL1 permits the oscillation of circadian gene expression. *Nat. Struct. Mol. Biol.* **17**, 1414–1421 [CrossRef](#) [Medline](#)
33. Aguilar-Arnal, L., Katada, S., Orozco-Solis, R., and Sassone-Corsi, P. (2015) NAD<sup>+</sup>-SIRT1 control of H3K4 trimethylation through circadian deacetylation of MLL1. *Nat. Struct. Mol. Biol.* **22**, 312–318 [CrossRef](#) [Medline](#)
34. Gau, D., Lemberger, T., von Gall, C., Kretz, O., Le Minh, N., Gass, P., Schmid, W., Schibler, U., Korf, H. W., and Schütz, G. (2002) Phosphorylation of CREB Ser142 regulates light-induced phase shifts of the circadian clock. *Neuron* **34**, 245–253 [CrossRef](#) [Medline](#)
35. Travnickova-Bendova, Z., Cermakian, N., Reppert, S. M., and Sassone-Corsi, P. (2002) Bimodal regulation of mPeriod promoters by CREB-dependent signaling and CLOCK/BMAL1 activity. *Proc. Natl. Acad. Sci. U.S.A.* **99**, 7728–7733 [CrossRef](#) [Medline](#)
36. Ye, W., Celiksoy, S., Jakab, A., Khmelinskaia, A., Heermann, T., Raso, A., Wegner, S. V., Rivas, G., Schwill, P., Ahijado-Guzmán, R., and Sönnichsen, C. (2018) Plasmonic nanosensors reveal a height dependence of MinDE protein oscillations on membrane features. *J. Am. Chem. Soc.* **140**, 17901–17906 [CrossRef](#) [Medline](#)
37. Ahijado-Guzmán, R., Prasad, J., Rosman, C., Henkel, A., Tome, L., Schneider, D., Rivas, G., and Sönnichsen, C. (2014) Plasmonic nanosensors for simultaneous quantification of multiple protein–protein binding affinities. *Nano Lett.* **14**, 5528–5532 [CrossRef](#) [Medline](#)
38. Ahijado-Guzmán, R., Menten, J., Prasad, J., Lambert, C., Rivas, G., and Sönnichsen, C. (2017) Plasmonic nanosensors for the determination of drug effectiveness on membrane receptors. *ACS Appl. Mater. Interfaces* **9**, 218–223 [CrossRef](#) [Medline](#)
39. Zor, T., De Guzman, R. N., Dyson, H. J., and Wright, P. E. (2004) Solution structure of the KIX domain of CBP bound to the transactivation domain of c-Myb. *J. Mol. Biol.* **337**, 521–534 [CrossRef](#) [Medline](#)
40. Hajizadeh, N. R., Franke, D., Jeffries, C. M., and Svergun, D. I. (2018) Consensus Bayesian assessment of protein molecular mass from solution X-ray scattering data. *Sci. Rep.* **8**, 7204 [CrossRef](#) [Medline](#)
41. Paz, J. C., Park, S., Phillips, N., Matsumura, S., Tsai, W.-W., Kasper, L., Brindle, P. K., Zhang, G., Zhou, M.-M., Wright, P. E., and Montminy, M. (2014) Combinatorial regulation of a signal-dependent activator by phosphorylation and acetylation. *Proc. Natl. Acad. Sci. U.S.A.* **111**, 17116–17121 [CrossRef](#) [Medline](#)
42. Scholz, J., Besir, H., Strasser, C., and Suppmann, S. (2013) A new method to customize protein expression vectors for fast, efficient and background free parallel cloning. *BMC Biotechnol.* **13**, 12 [CrossRef](#) [Medline](#)
43. Liu, H., and Naismith, J. H. (2008) An efficient one-step site-directed deletion, insertion, single and multiple-site plasmid mutagenesis protocol. *BMC Biotechnol.* **8**, 91 [CrossRef](#) [Medline](#)
44. Ye, W., Götz, M., Celiksoy, S., Tütting, L., Ratzke, C., Prasad, J., Ricken, J., Wegner, S. V., Ahijado-Guzmán, R., Hugel, T., and Sönnichsen, C. (2018) Conformational dynamics of a single protein monitored for 24 h at video rate. *Nano Lett.* **18**, 6633–6637 [CrossRef](#) [Medline](#)
45. Whitmore, L., and Wallace, B. A. (2004) DICHROWEB, an online server for protein secondary structure analyses from circular dichroism spectroscopic data. *Nucleic Acids Res.* **32**, W668–W673 [CrossRef](#) [Medline](#)
46. Sreerama, N., and Woody, R. W. (2000) Estimation of protein secondary structure from circular dichroism spectra: comparison of CONTIN, SELCON, and CDSSTR methods with an expanded reference set. *Anal. Biochem.* **287**, 252–260 [CrossRef](#) [Medline](#)
47. Blanchet, C. E., Spilotros, A., Schwemmer, F., Graewert, M. A., Kikhney, A., Jeffries, C. M., Franke, D., Mark, D., Zengerle, R., Cipriani, F., Fiedler, S., Roessle, M., and Svergun, D. I. (2015) Versatile sample environments and automation for biological solution X-ray scattering experiments at the P12 beamline (PETRA III, DESY). *J. Appl. Crystallogr.* **48**, 431–443 [CrossRef](#) [Medline](#)
48. Franke, D., Petoukhov, M. V., Konarev, P. V., Panjkovich, A., Tuukkanen, A., Mertens, H. D. T., Kikhney, A. G., Hajizadeh, N. R., Franklin, J. M., Jeffries, C. M., and Svergun, D. I. (2017) ATSAS 2.8: a comprehensive data

- analysis suite for small-angle scattering from macromolecular solutions. *J. Appl. Crystallogr.* **50**, 1212–1225 [CrossRef](#) [Medline](#)
49. Svergun, D. I. (1992) Determination of the regularization parameter in indirect-transform methods using perceptual criteria. *J. Appl. Crystallogr.* **25**, 495–503 [CrossRef](#)
50. Svergun, D. I., Petoukhov, M. V., and Koch, M. H. J. (2001) Determination of domain structure of proteins from X-ray solution scattering. *Biophys. J.* **80**, 2946–2953 [CrossRef](#) [Medline](#)
51. Franke, D., and Svergun, D. I. (2009) DAMMIF, a program for rapid *ab-initio* shape determination in small-angle scattering. *J. Appl. Crystallogr.* **42**, 342–346 [CrossRef](#) [Medline](#)
52. Volkov, V. V., and Svergun, D. I. (2003) Uniqueness of *ab initio* shape determination in small-angle scattering. *J. Appl. Crystallogr.* **36**, 860–864 [CrossRef](#)
53. Svergun, D. I. (1999) Restoring low resolution structure of biological macromolecules from solution scattering using simulated annealing. *Biophys. J.* **76**, 2879–2886 [CrossRef](#) [Medline](#)
54. Schneidman-Duhovny, D., Hammel, M., Tainer, J. A., and Sali, A. (2016) FoXS, FoXSDock and MultiFoXS: single-state and multi-state structural modeling of proteins and their complexes based on SAXS profiles. *Nucleic Acids Res.* **44**, W424–W429 [CrossRef](#) [Medline](#)
55. Svergun, D., Barberato, C., and Koch, M. H. J. (1995) CRY SOL: a program to evaluate X-ray solution scattering of biological macromolecules from atomic coordinates. *J. Appl. Crystallogr.* **28**, 768–773 [CrossRef](#)
56. Panjkovich, A., and Svergun, D. I. (2016) Deciphering conformational transitions of proteins by small angle X-ray scattering and normal mode analysis. *Phys. Chem. Chem. Phys.* **18**, 5707–5719 [CrossRef](#) [Medline](#)
57. Webb, B., and Sali, A. (2014) Comparative protein structure modeling using MODELLER. *Curr. Protoc. Bioinformatics* **47**, 5.6.1–5.6.32 [CrossRef](#) [Medline](#)
58. Pettersen, E. F., Goddard, T. D., Huang, C. C., Couch, G. S., Greenblatt, D. M., Meng, E. C., and Ferrin, T. E. (2004) UCSF Chimera- A visualization system for exploratory research and analysis. *J. Comput. Chem.* **25**, 1605–1612 [CrossRef](#) [Medline](#)
59. Valentini, E., Kikhney, A. G., Previtali, G., Jeffries, C. M., and Svergun, D. I. (2015) SASBDB, a repository for biological small-angle scattering data. *Nucleic Acids Res.* **43**, D357–D363 [CrossRef](#) [Medline](#)

**Structural and mechanistic insights into the interaction of the circadian transcription factor BMAL1 with the KIX domain of the CREB-binding protein**

Archit Garg, Roberto Orru, Weixiang Ye, Ute Distler, Jeremy E. Chojnacki, Maja Köhn, Stefan Tenzer, Carsten Sönnichsen and Eva Wolf

*J. Biol. Chem.* 2019, 294:16604-16619.

doi: 10.1074/jbc.RA119.009845 originally published online September 12, 2019

---

Access the most updated version of this article at doi: [10.1074/jbc.RA119.009845](https://doi.org/10.1074/jbc.RA119.009845)

Alerts:

- [When this article is cited](#)
- [When a correction for this article is posted](#)

[Click here](#) to choose from all of JBC's e-mail alerts

This article cites 59 references, 14 of which can be accessed free at <http://www.jbc.org/content/294/45/16604.full.html#ref-list-1>